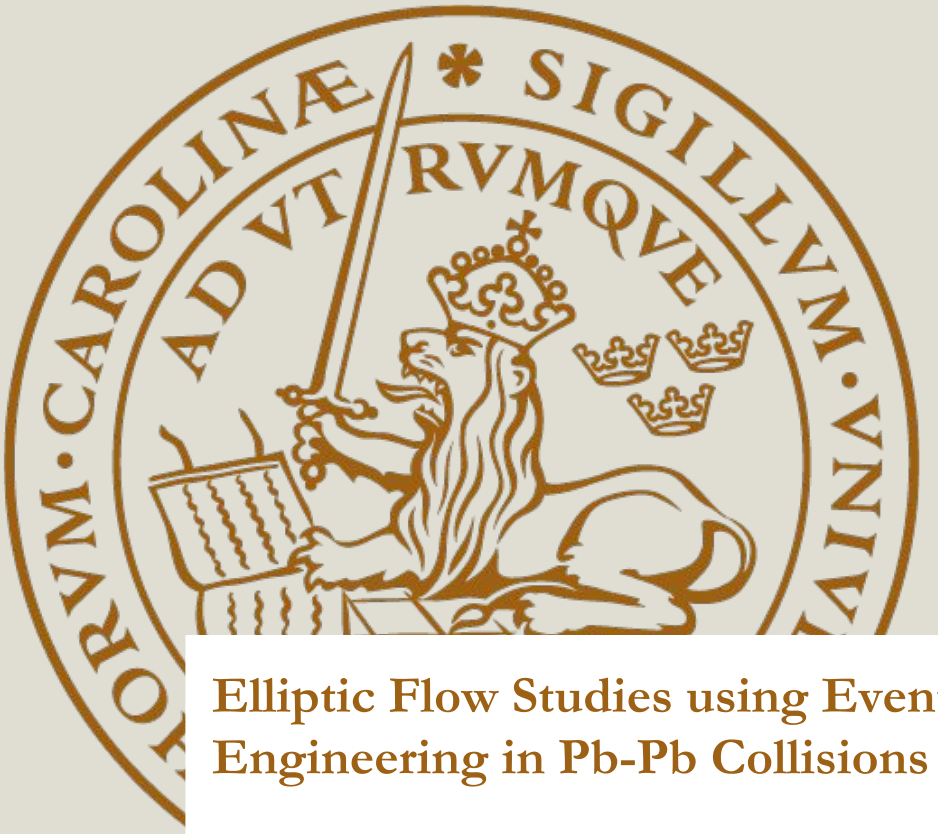

Elliptic Flow Studies using Event Shape Engineering in Pb-Pb Collisions at ALICE

Rickard Lydahl

Thesis Submitted for Degree of Master of Science
Project Duration: 4 Months

Supervised by Peter Christiansen

Lund University
Department of Physics
Division of Particle Physics
May 2017

Abstract

In ultra-relativistic heavy-ion collisions, QCD matter undergoes a phase transition to a strongly interacting Quark Gluon Plasma (QGP) where quarks and gluons are deconfined. The expansion of this plasma is well described by ideal hydrodynamics, suggesting that it behaves like a perfect, reversible, liquid. The particles emerging from the expansion are then highly correlated, showing collective behaviour originating from the plasma. This phenomenon is called collective flow and introduces key observables in the study of the QGP called flow harmonics v_n that reflect the initial anisotropies in the collision.

In this thesis, results on the elliptic flow harmonic v_2 are obtained using the Event Shape Engineering (ESE) technique applied to $\sqrt{s_{\mathrm{NN}}} = 2.76$ TeV Pb-Pb collisions at ALICE. By selecting events in a narrow centrality bin and in a certain flow interval, it is possible to control the initial geometry of the collision volume. Elliptic flow is calculated using the Q-cumulant method for two- and four-particle correlations. Results are also presented on the fluctuation and non-flow bias on the $v_2\{2\}$ and $v_2\{4\}$ transverse momentum distributions.

Populärvetenskaplig Sammanfattning

Denna avhandlingen presenterar en experimental studie till ett materietillstånd som existerade under de först mikrosekunderna efter Big Bang. Detta tillstånd kallas för *Kvark-Gluon-Plasma* och har lyckats bli återskapat i laboratorier genom att kollidera tunga atomkärnor med varandra. En sådan kollision uppnås genom att använda den stora partikelacceleratorer Large Hadron Collider (LHC) vid CERN som accelerar partiklar upp till hög-relativistiska hastigheter. För att kunna studera plasmats egenskaper behövs stora detektorsystem som omringar kollisionpunkten och läser av alla partiklar som faller ur kollisionen. Detektorn som används i denna analysen kallas för ALICE och är speciellt byggd för att titta på bly-bly kollisioner som producerar stora mängder partiklar.

Kvark-Gluon-Plasmat som produceras i de hög-energetiska bly-bly kollisionerna på CERN kräver temperaturer flera miljoner grader varmare än solens centrum samt en hög partikeldensitet för att bevaras. Tyvärr så är plasmat också väldigt ostabilt och kommer snabbt expandera utåt från kollisionspunkten och försvinna efter redan en mikroskopisk sekund ($\sim 10^{-23}$ s). Denna expansionen är väldigt väl beskriven av idealla hydrodynamiska modeller vilket innebär att plasmat beter sig som en reversibel vätska. Partiklarna som är producerade i plasmat är då väldigt korrelerade och visar ett kollektivt beteende som kallas *collective flow*. Detta fenomen leder till en karakteristisk kvantitet som kallas för *elliptic flow* som beskriver plasmats expandering från dens initiella geometri.

I denna avhandling så mäts elliptic flow från flera miljoner bly-bly kollisioner genom att titta på två- och fyra-partikelkorrelationer från plasmaexpansionen med ALICE detektorn. Anledningen att använda två sätt beror på att mätningen kommer inte bara bero på det globalla elliptic flow fenomenet men också kortdistans korrelationer som kommer från till exempel partikelsönderfall. Detta har en effekt som påverkar mätningen för två-partikelkorrelationer men är förstådd att inte påverka fyra-partikelkorrelationer. Det är då möjligt att få en bättre förståelse över dessa kortdistans korreleringar genom att jämnföra de två resultaten.

Elliptic flow mätningar med två- och fyra-partikelkorrelationer är tyvärr också påverkade av geometrifluktuationer som beskrivs av plasmats initiella volymvariationer när man jämför olika bly-bly kollisioner. Dessa fluktuationer skapar en positiv påverkan på elliptic flow mätningen med två-partikelkorrelationer och en negativ påverkan på mätningen med fyra-partikelkorrelationer. En lovande teknik som kallas *Event Shape Engineering* (ESE) har nyligen utvecklats som tyder på att man kan kontrollera vilken initiell geometri man vill studera. Denna avhandlingen applicerar ESE tekniken för att ta bort geometrifluktuationerna så att de beräknade elliptic flow värdena från två- och fyra-partikelkorrelationerna sammanfaller. Den kvarstående skillnaden är då i princip endast från kortdistans korrelationer och målet i denna avhandligen är att få en bättre förståelse över dessa effekter.

Acknowledgements

This thesis was my first work in heavy-ion physics and Quark Gluon Plasma phenomenon and would not have been possible without the help and inspiration from a lot of people. First and foremost I would like to thank my excellent supervisor Peter Christiansen. When you first presented the idea of elliptic flow and Event Shape Engineering I didn't completely understand what I was getting myself into but I'm glad you lead me into this fascinating research field. Thank you so much Peter!

A big thank you to the Lund ALICE group who took interest in my research and helped me whenever I got stuck. I am very grateful to you guys and the time we have spent together. Especially the trip to CERN during the ALICE week. I will never forget that trip; listening to people giving talks; hearing that Trump is the new president of the US; and all the singing we did at the karaoke bar. It has really been a wonderful experience.

Finally, I would like to thank my friends and family. Miaoxin, you deserve special thanks for being understanding and having to listen to all my frustrations. You're the best!

Contents

List of Acronyms

ALICE A Large Ion Collider Experiment

ATLAS A Toroidal LHC ApparatuS

CERN Conseil Européen pour la Recherche Nucléaire

ESE Event Shape Engineering

ITS Inner Tracking System

LHC Large Hadron Collider

PoI Particles of Interest

PP Participant Plane

RP Reference Particles

RHIC Relativistic Heavy-Ion Collider

SPD Silicon Pixel Detector

STAR Solenoidal Tracker At RHIC

TPC Time Projection Chamber

QCD Quantum Chromodynamics

QGP Quark Gluon Plasma

Work, work!
– Peon

1 Introduction

In a time before the planets, the stars and the galaxies existed it is believed that the Universe was made up of a hot and dense plasma known as a Quark Gluon Plasma (QGP). This state of matter formed within the first few milliseconds of the Big Bang and filled the entire Universe. To study the structure of the plasma and the strong force at play one has to achieve these extreme conditions of the early Universe inside the laboratory.

With the Large Hadron Collider (LHC) at CERN, the European organization for Nuclear Research, one can achieve incredibly dense matter states with temperatures over one-hundred-thousand times hotter than the center of the sun, to recreate the Quark Gluon Plasma. This is done by accelerating Pb nuclei in opposite directions up to ultra-relativistic speeds in the 27 kilometre long LHC tunnel and colliding them. The collision causes the formation of a QGP that lasts only for a tiny fraction of a second ($\sim 10^{-23}$ s) before expanding and cooling down [1].

The ALICE detector, an abbreviation of 'A Large Ion Collider Experiment', is an extremely sensitive detector system at the LHC, specifically designed to study these lead-lead collisions. With it, one can track the particles that emerge from the collision point and study the properties of the QGP. In this thesis, event data from lead-lead collisions recorded during 2010 with ALICE are used with the aim to analyse one of the plasma's collective properties known as *elliptic flow*.

1.1 Quark Gluon Plasma

Quark Gluon Plasma is a phase of matter, like the solid and liquid phases of matter, but instead of consisting of atoms it is made up of deconfined quarks and gluons (two types of sub-atomic particles). The plasma is considered a *new* phase of matter in the sense that it has only been produced in high energy heavy-ion collisions dating back a few decades. The initial discovery was made using the Relativistic Heavy Ion Collider at Brookhaven, where gold-gold collisions were investigated at large collision energies [2; 3]. After formation, the QGP will quickly expand and cool off until hadronization occurs. It is by studying these hadrons, using large detector systems enveloping the collision point, that the properties of the plasma are studied.

One surprising property of the plasma that has been observed is that the expansion behaves similarly to an almost ideal fluid [4]. This means that the expansion is spatially reversible and that it can be described by hydrodynamical models where local pressure gradients drive the expansion. This reversibility also suggests that there are strong particle correlations manifesting from the medium. This phenomenon is an important characteristic of the QGP and is known as *collective flow*. A theoretical description of the plasma and its constituents is presented in Chapter 2.

1.2 Heavy Ion Collisions and the ALICE Detector

A high-energy heavy-ion collision has some similarities with a miniature version of the Big Bang. It is achieved by accelerating heavy ions up to ultra-relativistic speeds and then colliding them. This collision event creates an environment that is trillions of degrees Celsius and extremely particle dense. It is under these conditions that nuclear matter undergoes a phase transition to a strongly interacting QGP, similar to the early Universe [5]. Figure 1. shows an illustration of the evolution of the Universe with indications of the pre-nuclei conditions that heavy ion collisions at RHIC and LHC achieve.

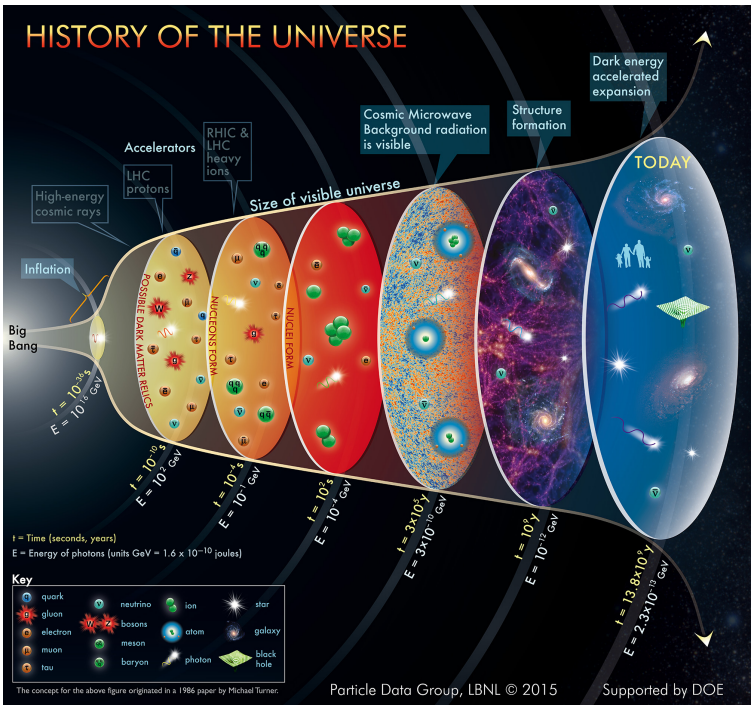

Figure 1: Scheme of the evolution of the Universe in the Big Bang scenario. A state of QGP existed before nuclei were formed [6].

At the LHC, the main detector designed for studying heavy-ion collisions is ALICE. It is a large detector system that surrounds one of the LHC collision points and is extremely particle sensitive, which is necessary to be able to analyse the large number of particles emerging from a Pb-Pb collision. In this thesis, data recorded during 2010 of Pb-Pb collisions at a centre-of-mass energy of $\sqrt{s_{\mathrm{NN}}} = 2.76$ TeV is used. A detailed description of the ALICE detector and its sub-detector systems is presented in Chapter 4.

To be able to discuss the aim of this thesis it is necessary to first present some standard concepts in heavy ion collisions (strict definitions are made in Chapter 3). To start with, one defines the reaction plane of a collision as being spanned by the axis along the beamline and the impact parameter vector. Here, the impact parameter is the distance between the centers of the two colliding nuclei. When the impact parameter is small one is looking at central collisions and when it is large one is looking at peripheral collisions. One also defines the azimuthal plane, spanning over 2π azimuthal angle, perpendicular to the beam-axis.

1.3 Aim of This Thesis

The number of experimental observables that are used for interpretation of QGP phenomenon is quite limited due to only seeing the particle remnants of the plasma with a detector. Therefore, having a good understanding of how these observables behave is essential to understanding the QGP evolution in heavy ion collisions. This thesis aims to study the behaviour of one of the observables related to the collective behaviour of the QGP – elliptic flow. In the following sections, a brief overview of elliptic flow and how it will be studied in this thesis is presented.

1.3.1 Elliptic Flow

There are several orders of flow stemming from strong collective effects in the QGP. Elliptic flow is the second order of flow and is strongest in peripheral heavy ion collisions [7]. In these types of collisions, the initial geometry of the two nucleon's collision volume is not symmetric, as shown in Fig. 2. This spatial anisotropy leads to a faster expansion of the medium in the reaction plane than in the plane perpendicular to this. Elliptic flow is then a measure of how asymmetric the final particle distribution is in the azimuthal plane [7]. The elliptic flow has a strong dependence on the impact parameter and one therefore typically restricts the analyses to narrow centrality classes. The measured elliptic flow arising from the collision volume is also directly proportional to the eccentricity. A detailed description of flow phenomena (elliptic flow in particular) as well as previous results are presented in Section 3.4.

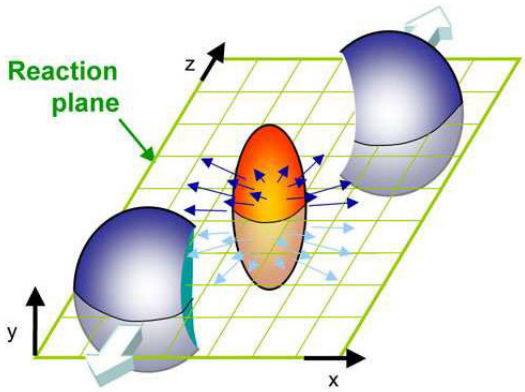

Figure 2: Illustration of the asymmetric collision volume in a heavy-ion collision [8].

Measuring elliptic flow can be done in several ways. In this thesis, elliptic flow is measured using 2- and 4-particle correlations, where one only needs to know the angles of the emitted particles and one can avoid calculating a common event plane (an event estimate of the reaction plane). However, the idea is that the particles still remain correlated through the event plane due to the collective behaviour of the QGP expansion.

The reason for calculating the 4-particle correlations alongside the 2-particle correlations is that there are particle correlations not only due to flow but also correlations arising from other phenomena such as resonance decays and particle jets. These correlations are called *non-flow* and are mostly correlations between few particles that introduce a bias in the measured flow. For 4-particle correlations it is believed that non-flow effects are almost completely eliminated. Therefore, by comparing elliptic flow measurements of second- and fourth-order particle correlations it is possible to better understand these non-flow effects.

Elliptic flow measurements are, unfortunately, not only biased by non-flow correlations, but also by event-by-event *fluctuations* in the initial geometry of the collision volume. It is known that the elliptic flow estimates from 2-particle correlations are enhanced by the fluctuations while 4-particle correlations are suppressed by the fluctuations [9]. However, a recent method, presented in the next section, has been developed that makes it possible to select events based on their initial geometry which can minimize the initial geometry fluctuations.

1.3.2 Event Shape Engineering

Event Shape Engineering (ESE) is a technique that lets one control the initial geometry of the heavy-ion collision volume [10]. This is done by making use of the flow vector (defined in Section 3.4) which is proportional to the eccentricity of the event. The main principle of ESE is then to make use of this proportionality relation to select events where the flow vector falls in a narrow range, making the events have very similar initial geometry.

The main goal of this thesis is to apply the ESE method on ALICE Pb-Pb collision data so that the analyzed events fall into different classes with similar initial geometry. This has the effect of minimizing the fluctuations that bias the elliptic flow measurement when using 2- and 4-particle correlations. Then, by studying the difference between the elliptic flow estimates from the two correlators, one hopes to find a better understanding of how non-flow effects bias the flow measurement. Currently, it is believed that higher order correlations almost completely remove non-flow. For instance, a non-flow source from a resonance decaying into two particles would not bias the 4-particle correlation. The ESE method and previous results obtained with ALICE are presented in Chapter 3.4.

2 Theoretical Description of the Quark Gluon Plasma

2.1 Quarks, Gluons and the Standard Model

The quarks and gluons that make up the plasma in ultra-relativistic heavy-ion collisions are both *elementary* particles. These are types of fundamental particles with no known internal structure and are therefore often referred to as the building-blocks of our Universe. The elementary particles and their interactions are collectively described by the Standard Model, a framework used in particle physics that has been developed since the 1960s when the electromagnetic and weak interactions were unified into the electroweak interaction [11]. From its inception, the Standard Model has withstood many stringent experimental tests as well as predicted the existence of particles before their discovery.

The elementary particles, as described by the Standard Model, each have a set of quantum numbers that describe what their properties are. The quark, for instance, is a *fermion* and therefore has a spin magnitude of $s = 1/2$. Spin is a quantum number that is associated with the intrinsic angular momentum of a particle. All fermions have half-integer spin and obey the Pauli exclusion principle, stating that no two fermions can occupy the same quantum mechanical state at the same time (at least one quantum number is different) [12]. A list of the Standard Model fermions is presented in Table 1 with masses given in natural units[1] by the Particle Data Group [13].

Fermions are divided up into quarks and leptons, with a total of six particles ("flavors") each divided up into three generational pairs. The properties of the fermions going from one generation to another all remain the same except for the particle masses. Normal matter, consisting of atoms, is constructed from particles in the first generational pairs of the quarks and leptons. As an example, the hydrogen atom is made up of one electron orbiting a nucleus consisting of a single proton. The proton is a composite particle made up of up and down quarks described by the quark model, independently developed by M. Gell-Mann and G. Zweig in 1964 [14]. Experimental proof of the quark model was achieved in 1969 with the Stanford Linear Accelerator by looking at deep inelastic scattering experiments [15], where a point-like internal structure was seen in protons.

[1]Natural units imply $c = \hbar = 1$, where c is the speed of light and $\hbar$ is the reduced Planck's constant.

Table 1: The fermions of the Standard Model.

	Fermions	Short-hand	Generation	Charge	Mass
Quarks	up	u	I	+2/3	2.4 MeV
	down	d	I	-1/3	4.8 MeV
	charm	c	II	+2/3	1.27 GeV
	strange	s	II	-1/3	104 MeV
	top	t	III	+2/3	171.2 GeV
	bottom	b	III	-1/3	4.2 GeV
Leptons	electron	e	I	+1	0.511 MeV
	electron neutrino	ν_e	I	0	<2.2 eV
	muon	μ	II	+1	105.7 MeV
	muon neutrino	ν_μ	II	0	<0.17 MeV
	tau	τ	III	+1	1.77 GeV
	tau neutrino	ν_τ	III	0	<15.5 MeV

The quark model introduces new layers of categorization, where for instance particles built up by quarks are called *hadrons*. A hadron made up of three quarks is called a *baryon* and a hadron made up of a quark and an anti-quark is called a *meson*. A proton is an example of a baryon consisting of two up and one down quark, short-handed (uud). The π^- (pion) is an example of a meson built by one down quark and one anti-up quark ($\mathrm{d\bar{u}}$), where $\bar{\mathrm{u}}$ is just an up quark with opposite electric charge. All elementary particles in the Standard Model have their own associated anti-particles, but in some cases a particle is its own anti-particle. All hadrons, as described by the quark model, are characterized by a quantum number given by:

$$B = \frac{1}{3}(n_q - n_{\bar{q}}) \tag{1}$$

where B is called the *baryon number* and n_q ($n_{\bar{q}}$) is the number of quarks (anti-quarks). Baryons (qqq) have a baryon number of +1 while anti-baryons ($\bar{\mathrm{q}}\bar{\mathrm{q}}\bar{\mathrm{q}}$) have a baryon number of -1. From the definition, mesons always have a baryon number of 0.

The remaining particles in the Standard Model that are not fermions are the *bosons*. Bosons differ from fermions in that they have integer spin and do not obey the Pauli exclusion principle, meaning that they can stack up in a single quantum state. A list of the Standard Model bosons is shown in Table 2. The bosons serve a special purpose as the mediators of the different forces described by the Standard Model. For example, the photon is the mediator of the electromagnetic force and can couple to all electrically charged particles. An electromagnetic interaction between two electrons is then treated as a photon being emitted from one electron and absorbed by the other electron. Similar situations are true for the two other forces. The weak force is mediated by the massive bosons $\mathrm{W}^\pm$ and Z, and couples to *weak isospin* defined by the quantum number T_3. The significance of the weak force is that it allows for quarks to change flavors, *i.e.* transforming from one type of quark into another. The (u,c,t) quarks have $T_3 = 1/2$ and can transform into (d,s,b) quarks which have $T_3 = -1/2$. The opposite case is also true but a quark can not transform into another quark with the same T_3.

The force most relevant for this thesis is the strong force and is mediated by the gluon which couples to *color charge*. The strong force and some of its key phenomena

Table 2: The bosons of the Standard Model.

Force	Boson	Charge	Mass	Spin
Electromagnetic	Photon	0	0	1
Weak	$W^{\pm}$, Z	± 1, 0	80.4 GeV, 91.2 GeV	1
Strong	Gluon	0	0	1
–	Higgs	0	125.09 GeV	0

will be discussed in the next section. However, before continuing, there are two things that are worth mentioning. First, the Higgs boson is not a force mediating boson like the spin 1 bosons (vector bosons). The Higgs is a spin 0 particle (scalar boson) which serves the purpose of providing the mass to the other particles in the Standard Model through the Higgs mechanism, and was introduced to explain the symmetry breaking of the electroweak force [16]. The second thing that is worth mentioning is that gravity is nowhere mentioned in the Standard Model[2]. This commonly known force has proven to be very difficult to incorporate into the model. However, it is believed that the force of gravity is also mediated by a boson called the graviton, similar to the other forces.

2.2 Quantum Chromodynamics

Quantum Chromodynamics (QCD) is the theory describing the strong interaction in the Standard Model. It has already been mentioned that the massless gluon acts as the force mediator and couples to color charge. Quarks are the only fermions that carry color charge and can therefore interact through all the fundamental forces previously mentioned. A quark can carry either a red, green or blue (r,g,b) color charge and an anti-quark can carry either of the corresponding anti-colors ($\bar{\text{r}}$,$\bar{\text{g}}$,$\bar{\text{b}}$). The concept of color charge was introduced by Oscar W. Greenberg [17], shortly after the quark model had been proposed, as an explanation for why quarks with otherwise the same quantum state can coexist inside a hadron.

A unique feature of the strong interaction is that its force mediator, the gluon, also carries color charge. There are 8 possible color-anticolor states that the gluon can have. A direct consequence of this is that the gluon can self-interact, which leads to a phenomena known as *anti-screening* [18]. The concept of anti-screening is best explained alongside another phenomena called *screening* which also features in QCD.

Consider the Feynman diagrams shown in Fig. 3, time goes horizontally from left to right. These are called loop diagrams and the left figure shows a propagating quark emitting a virtual gluon that fluctuates into a quark-antiquark pair for a brief moment before being absorbed by another quark. The quark-antiquark loop will generate a color field corresponding to the particle's color charges. This gives rise to *vacuum polarization effects* where the direction of the field is opposite to the color field of the scattered quark. This results in a smaller total net field and is referred to as the screening effect.

In QCD, there is also another vacuum polarization correction that is due to the gluon self-interaction. Fig. 3 right, shows two quarks scattering with a gluon loop fluctuation. The color fields due to the gluon loop gives rise to anti-screening. This is a dominating effect compared to the secondary screening effect, where now the subfield generated by the

[2]The gravitational force can be neglected in particle physics as its magnitude is around 40 orders weaker than the strong force.

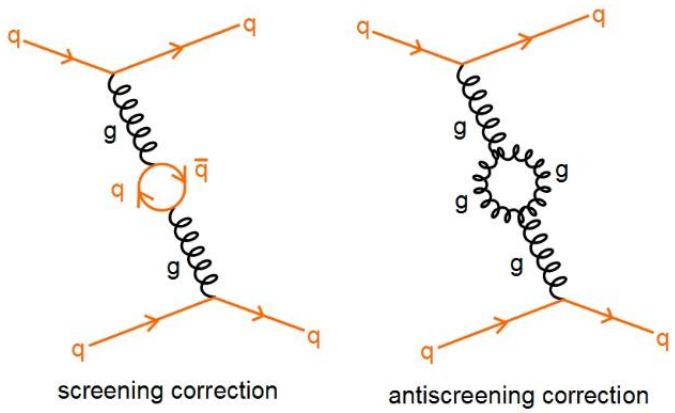

Figure 3: QCD screening and anti-screening concepts [19].

gluon loop runs parallel to the field of the scattered quark. The result is that in QCD the effective color charge is overall enhanced by the screening and anti-screening concepts. It is not only scattering diagrams that contribute but propagating quarks can spontaneously emit gluons to form loops of quark-antiquark (gluon) pairs having significant screening (anti-screening) effects.

In the above scattering diagrams, the measured response of the strong coupling constant α_S is dependent on the wavelength that is probed, with *i.e.* the size of the interaction. The momentum transfer Q of the interaction is also related to the probing wavelength and one therefore look at α_S as a function of Q^2 to take into account higher order loop diagram corrections to perturbative QCD calculations. The effective coupling constant is given by

$$\alpha_s = \frac{g_s^2}{4\pi}, \tag{2}$$

where g_s is the strong coupling strength and is dependent on the mass scale μ. At the QCD scale ($\mu = \Lambda_{\text{QCD}} \simeq 200$ MeV) leading order perturbative QCD calculations give

$$\alpha_S(Q^2) \simeq \frac{12\pi}{(11N_C - 2N_f)\ln(Q^2/\Lambda^2_{\text{QCD}})}, \tag{3}$$

where $N_C = 3$ is the number of colors and emerges from anti-screening loops, $N_f = 6$ originates from the screening loops and represents the number of quark flavors [20]. The factor $(11N_C - 2N_f)$ is then positive and explains why anti-screening dominates over screening in QCD. From the above equation it is also seen that α_S is small at large momentum transfer and large at small momentum transfer. This means that the strong interaction becomes weaker at short distances and stronger at large distances, a phenomena called *asymptotic freedom*. A summary of measurements of the running coupling constant $\alpha_S(Q)$ for different experiments is shown in Fig. 4.

The concept of *confinement* emerges from the increasing strength of the strong coupling constant as distances grow. If a quark-antiquark pair (meson) is separated, the interaction between them becomes stronger and according to the Lund String Model the gluon field between them will shape like a one-dimensonal string [22]. The energy stored in this field is $\sim$1 GeV/fm and at a certain distance the string will break, creating a new quark-antiquark pair. The final result is that one meson has become two mesons. The confinement

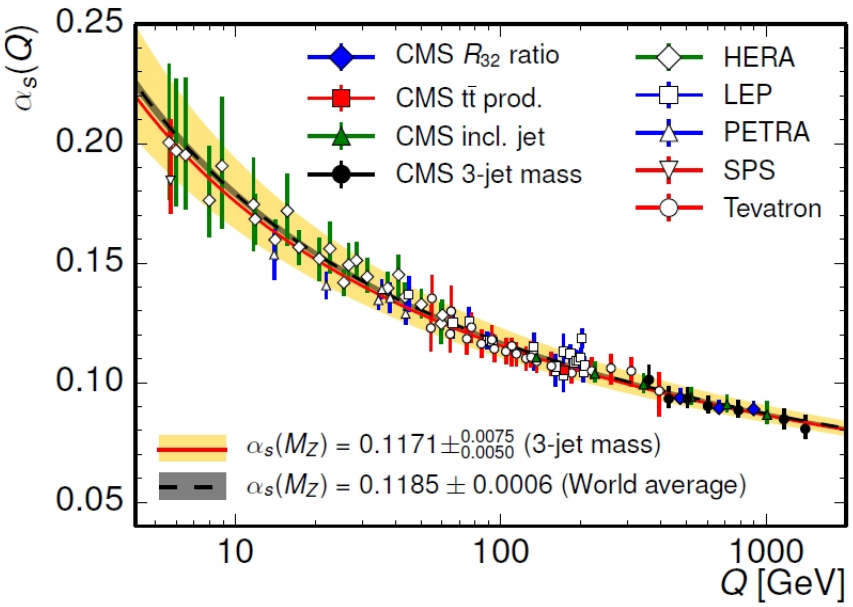

Figure 4: Measurements of α_S as a function of momentum transfer for different experimental probes. QCD predictions for $\alpha_S(M_Z)$ using Z boson mass M_Z are shown [21].

phenomena then explains why quarks and gluons can only be seen as composite particles such as mesons and baryons, and not as free particles.

2.3 The Strongly Interacting Plasma

A phase transition from hadrons into a plasma of deconfined quarks and gluons was first suggested to exist by T. D. Lee in 1974 [23]. The name Quark Gluon Plasma was introduced in 1978 by Edward Shuryak with the realisation that thermal fluctuations of gauge fields can lead to color screening [24], similar to the screening effect of mobile charges in an electromagnetic plasma[3]. At the same time it was also suggested that heavy-ion collisions could produce a particle- and energy-dense environment where screening effects cause hadrons to *melt* and form a QGP [25]. This makes the partons (quarks and gluons) unbounded and free to interact with other partons in a phenomenon known as *deconfinement*.

The QCD phase transition from hadronic matter to a QGP is illustrated in the phase diagram shown in Fig. 5. The phase transition occurs around an energy density of $\epsilon \simeq 1$ GeV/fm^3 and at a critical temperature $T_C \simeq 160$ MeV (corresponding to $\sim 10^{12}$ Kelvin) [26]. A phase transition that occurs at low net baryon density, to the left of the critical point T_C, is a second order phase transition [27], meaning that the mixture of hadrons melting to free partons experience a smooth transition. This type of transition occurs in the heavy-ion collisions at RHIC and LHC. To the right of T_C, for high net baryon density, the transition has a strict boundary and is a first order phase transition.

[3]This phenomena is called *Debye screening*, where the force between two charges is screened by the polarized charges between them.

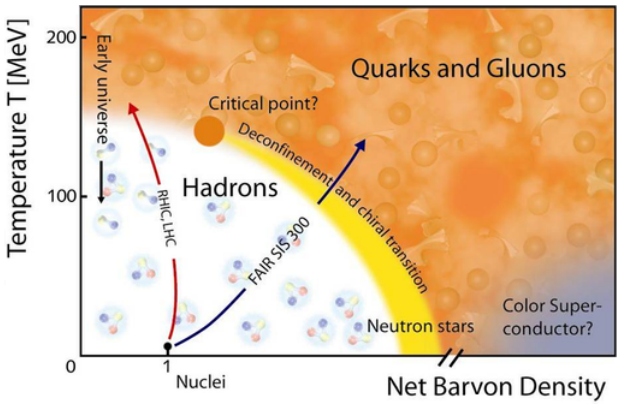

Figure 5: QCD matter phase diagram in temperature and net baryon density. Hadronic matter transitions to QGP for sufficient temperature and net baryon density. Indication of the evolution of the early universe as well as achievable conditions with RHIC and LHC are also shown [28].

3 Heavy-Ion Physics

In this chapter, the main concepts of heavy-ion physics used in this thesis are presented. First, some key kinematic variables that are used throughout this work are presented. Then the concepts of impact parameter and centrality are defined. Finally, a discussion of the QGP formation and its different stages of evolution in the collision is presented. Before continuing, one important definition in heavy ion physics is the multiplicity M which is just the number of outgoing particles from a collision. In this thesis it will refer to the number of *charged* particles coming from the collision which is a distinction that is often made.

3.1 Kinematic Variables

In high energy physics one makes specific variable definitions in order to better understand particle collisions. Some of the key variables used in this thesis are presented here. For a deeper discussion and more definitions refer to *e.g.* R. Sahoo [29]. Note that natural units are used in the expressions presented below. That is $c = 1$, where c is the speed of light.

3.1.1 Transverse Momentum

One often divides the momentum up into a longitudinal momentum component p_z, defined along the beam axis, and a transverse momentum component, defined by:

$$p_{\mathrm{T}} = \sqrt{p_x^2 + p_y^2}. \tag{4}$$

This is a convenient choice since the transverse momentum is Lorentz invariant, and is always associated with physics that happened in the particle collision. The p_z component is less important as a particle's momentum in this direction could be left over momentum from the beam particles. Looking at p_{T}-spectra therefore gives a relatively clean sample of interesting physics that happened due to particle interactions. In the context of measuring elliptic flow as a function of p_{T}, the distribution is generally divided into three

different categories: low-p_{T} ~[0,3] GeV/c, intermediate-p_{T} ~[3,5] GeV/c and high-$p_{\mathrm{T}} \gtrsim 5$ GeV/c [30].

3.1.2 Collision Energy

The collision energy is the total energy available from a particle collision in the centre-of-mass frame and can be calculated using the four-momentum vector $p^{\mu} = (E, -\boldsymbol{p})$, where E is the particle energy and $\boldsymbol{p}$ is the three-momentum. The total four-momentum of a system of colliding particles is a conserved quantity.

For two colliding particles of the same mass and energy with opposite three-momentum ($p_1 = (E, \boldsymbol{p})$ and $p_2 = (E, -\boldsymbol{p})$), the centre-of-mass energy can be calculated by squaring the total four-momentum:

$$\begin{aligned} p_{\mu}p^{\mu} &= (p_1 + p_2)^2 \\ &= p_1^2 + p_2^2 + 2p_1p_2 \\ &= (E^2 + |\boldsymbol{p}|^2) + (E^2 + |\boldsymbol{p}|^2) + 2(E^2 - |\boldsymbol{p}|^2) \\ &= 4E^2 = E_{\mathrm{CM}}^2 \equiv s, \end{aligned} \tag{5}$$

where $E_{\mathrm{CM}} = \sqrt{s}$ is the centre-of-mass energy. It is clear that in this type of collision, the centre-of-mass energy is given by $\sqrt{s} = 2E$ which is just twice the beam energy. The use of $\sqrt{s}$ to define the centre-of-mass energy is standard in proton-proton collisions but differs in heavy ion collisions. Typically one also uses $\sqrt{s_{\mathrm{NN}}}$ where NN implies energy per colliding nucleon pair[4]. This makes it convenient to compare energy scales across experiments that are colliding different types of ions.

3.1.3 Rapidity and Pseudorapidity

Rapidity and pseudorapidity are two useful variables in high energy physics. The rapidity y is defined as:

$$y = \frac{1}{2} \ln \left(\frac{E + p_z}{E - p_z} \right) \tag{6}$$

and is a *dimensionless* quantity used to represent a particle's movement along the beam-line. When y is positive, it indicates that the particle is moving in the forward direction while a negative value represents the particle's movement in the backward direction. This definition is similar to that of the magnitude of velocity but has the convenience of being additive under a Lorentz boost, which is not the case for velocities. The main advantage of this is that the general shape of rapidity-distributions remain unchanged when going from the the centre-of-mass frame to the laboratory-frame [29], making it very useful for studying particle production in collisions. This is especially important when relating collision and fixed-target results.

To be able to calculate the rapidity it is necessary to know the energy of the particle, which can sometimes be measured directly in a detector system. Indirect measurements can also be done by identifying the momentum and mass of the particle and using the relativistic energy-momentum relation given by:

$$E = \sqrt{m^2 + p^2}. \tag{7}$$

[4]Defined as $\sqrt{s_{\mathrm{NN}}} = \sqrt{s}/A$, where A is the atomic number.

However, in some cases it is not possible to measure the energy or momentum due to, *e.g.*, detector limitations. In such a case, one can make the assumption that when a particle is traveling at relativistic speeds, the transverse momentum is much larger than the mass, $p_{\mathrm{T}} \gg m$, and the particle energy is then simply given by its momentum. From this assumption it follows that

$$y \approx \frac{1}{2} \ln \left(\frac{p + p_z}{p - p_z} \right) = \frac{1}{2} \ln \left(\frac{1 + \cos\theta}{1 - \cos\theta} \right) = -\ln[\tan \theta/2] \equiv \eta, \tag{8}$$

where θ is the polar (or emission) angle and η is the pseudorapidity. Note that the pseudorapidity only has angular dependence and does not require the momentum or energy of the particle to be measured. The approximation $y \approx \eta$ holds for relativistic velocities or for large emission angles, $\theta \gg 1 - \gamma$, where γ is the Lorentz factor. The pseudorapidity for different values of emission angle is shown in Fig. 6.

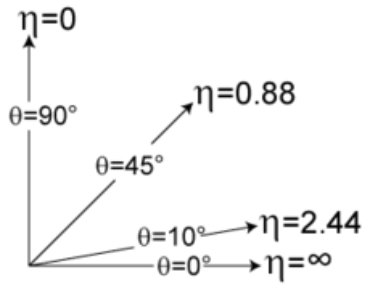

Figure 6: Pseudorapidity values corresponding to different emission angles, where $\theta = 0^\circ \rightarrow \eta = \infty$ is along the beam direction and $\theta = 90^\circ \rightarrow \eta = 0$ is perpendicular to the beam.

Pseudorapidity is an essential variable in this thesis and is used for selecting and accepting particle tracks recorded by the ALICE detector. In Section 5.4 the concept of using rapidity-gaps in flow analysis is presented, which allows for measuring elliptic flow with the ESE method in several ways.

3.2 Collision Geometry

In a heavy-ion collision one defines the impact parameter b as the distance between the centers of the two colliding nuclei. Fig. 7 illustrates a collision of two ultra-relativstic heavy ions in the centre-of-mass frame where both ions are Lorentz contracted in their direction of motion. The nucleons that participate in at least one inelastic collision are called the *participants* and the remaining, non-interacting, nucleons are called *spectators*. The impact parameter has an inverse relation with the collision volume meaning that the most central hits give rise to the largest collision volumes and the smallest impact parameters. These central collisions are the most particle dense and are therefore expected to have the most pronounced effects of QGP formation. As a consequence of the large particle density, there will be many particles produced in the collision (large multiplicity), requiring detectors with high granularity and sensitivity to be able to study heavy-ion collisions. Knowing the centrality of an event is essential to studying heavy-ion collisions as observables may vary greatly from central collisions to the most peripheral ones.

Unfortunately, the impact parameter can not be measured directly. Instead, one classifies the centrality of an event by its multiplicity, which on average increases monotonically

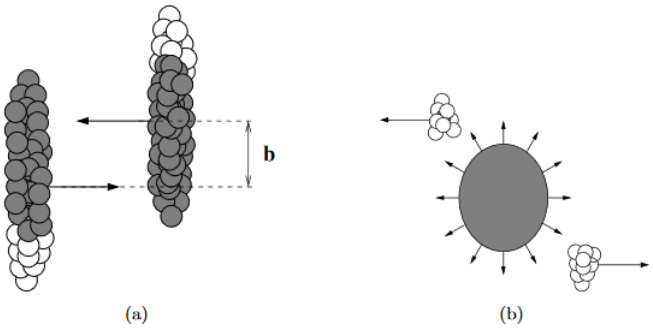

Figure 7: Illustration of a heavy-ion collision in the centre-of-mass frame [31]. (a) Definition of the impact parameter. (b) The participants and spectators.

with the number of participants at both forward rapidity and midrapidity [32]. For events with large b (peripheral collision), small multiplicity is expected at midrapidity and a large multiplicity from spectators at beamrapidity. In central collisions, the opposite case is expected, where there is large multiplicity at midrapidity and only a few spectators at beamrapidity. By measuring the multiplicity distribution and comparing to Monte Carlo simulations from a Glauber model it is possible to define the centrality classes, as shown for ALICE in Fig. 8 [33]. Here, the multiplicity is represented by the signal amplitude of the VZERO detector which is discussed in Section 4.2. A Glauber model is used to relate the detector measurement with the variables of the initial state geometry, such as the impact parameter and the shape of the collision region. This is done by assuming a negative binomial distribution for the particle production in the model and fitting it to the data. For each of the centrality classes it is possible to calculate the mean values of the Glauber quantities, such as the number of participants and spectators. The definition of centrality is then done as a percentile number, where 0% are the most central events and 100% are the most peripheral ones.

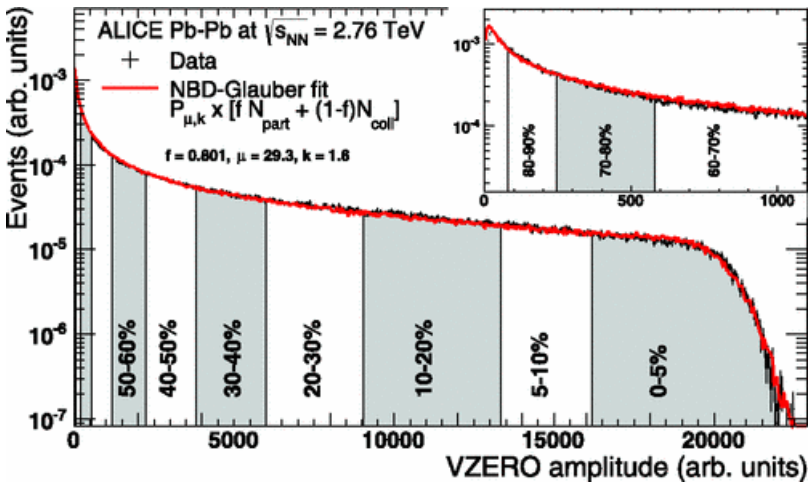

Figure 8: Centrality determination in ALICE. The distribution of the sum of VZERO signal amplitudes is shown with a negative binomial distribution Glauber fit (red line). The centrality classes are divided by vertical lines and alternating shade [34].

3.3 Quark Gluon Plasma Evolution

After the QGP has been formed it will rapidly expand in an explosion-like manner. This expansion is well described by hydrodynamical models using local pressure gradients that drive the expansion, and has been shown to behave like an almost ideal liquid [4]. This means that the shear viscosity is much smaller than the entropy density, indicating that the expansion is almost reversible and that there are strong particle correlations referred to as collective flow originating from the QGP. The rapid expansion of the plasma will cause the temperature to drop below the critical temperature needed to maintain the QGP phase, causing the quarks and gluons to hadronize.

The evolution of the plasma produced in a heavy ion collision can be divided up into several stages [35]. They are the pre-equilibrium, expansion, hadronization, and freeze-out stages. The pre-equilibrium stage describes the production of a highly excited fireball from the initial partonic collisions. The fireball quickly establishes local thermal equilibrium due to high frequency collisions and achieves a locally thermalized state. The next stage of the QGP evolution is the expansion phase which is driven by local pressure gradients as already mentioned. The expansion causes a decrease in the energy density that eventually reaches below the conditions necessary for maintaining a QGP. This leads to the hadronization process where all quarks and gluons will form into hadronic matter. However, there remains a possibility that local equilibrium can be established from hadrons colliding frequently. In the end, the ongoing expansion will cause the hadrons to stop interacting and is referred to as the freeze-out stage.

The freeze-out is the last step in the QGP evolution before the particles enter the detectors and consists of the chemical and the kinetic freeze-out. The chemical freeze-out is characterized by the fact that elastic collisions still occur at this stage, making it possible to still have local equilibrium. This is because the rate at which inelastic collisions occur decreases faster than the elastic interaction rate when temperature and density drops[5]. Chemical freeze-out is then defined as the point where inelastic collisions stop and the abundance of different hadron types are fixed. When the particle composition recorded by ALICE is fitted with a thermal model, a chemical temperature T_{ch} in the range 146-166 MeV is obtained, which is very close to the expected phase transition at $T_C \simeq 160$ MeV (see Section 2.3) [36]. The kinetic freeze-out occurs when only elastic collisions remain, changing the momenta of the particles. It stops when the average distance between the hadrons is larger than the range of the strong force and when the collision frequency diminishes so that local equilibrium can not be maintained.

3.4 Flow

In this section, the flow phenomenon seen in heavy-ion collisions is presented. The brief description of elliptic flow in Section 1.3.1 will be further detailed in this section. The concept of flow originates from collective effects occurring in heavy-ion collisions. If no QGP is formed during the collision it is expected that the particle distribution in azimuthal angle ϕ is homogeneous. This means that each nucleon-nucleon collision is independent and that the particles are emitted in random directions. However, if there is a medium formed, a non-isotropic spatial distribution of particles is expected.

[5]An elastic collision has the same initial and final state particles: A + B → A + B. This is not true for inelastic collisions where final state particles are different

3.4.1 Radial Flow

Radial flow is the first order of flow and originates from the radially expanding medium where hadrons are boosted by an average velocity $\mathbf{v}$ when going from their rest frame to the laboratory frame. This Lorentz boost causes a mass hierarchy where a heavier hadron at rest in the local QGP frame will gain a larger momentum than a lighter hadron according to $\mathbf{p} = \gamma m\mathbf{v}$. There is therefore a general shift of particle abundance from low p_{T} to high p_{T}. Results from ALICE of this phenomenon are shown in Fig 9, where the particle yields in the transverse momentum spectra are compared in proton-proton (pp) collisions and Pb-Pb collisions. The shapes differ quite clearly between the two collision types with Pb-Pb collisions having less step slopes. The mass hierarchy is clearly seen in the (anti)proton results which have a smaller abundance (relative to the lighter pions) at low p_{T} in Pb-Pb collisions compared to pp collisions. At intermediate and high p_{T} there is an increase in proton yield as expected from radial flow.

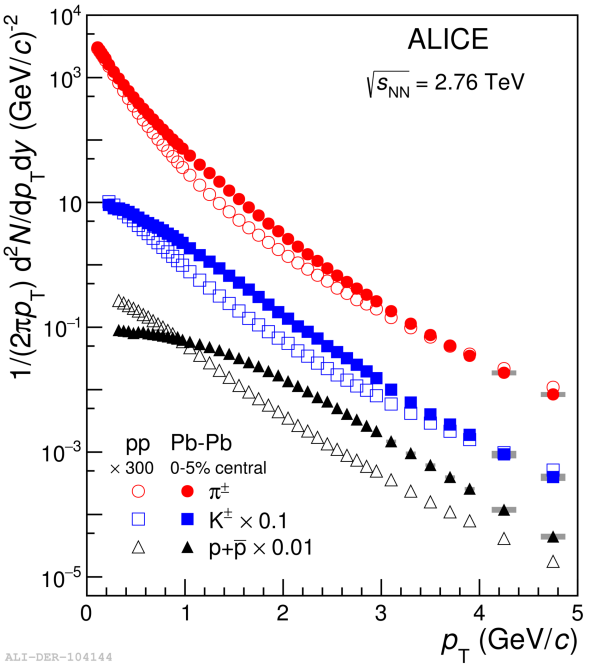

Figure 9: Charged pion, kaon and (anti)proton production in pp and Pb-Pb collisions at $\sqrt{s_{\mathrm{NN}}} = 2.76$ TeV. The pp spectra is scaled for better comparison [37].

3.4.2 Anisotropic Flow

The higher orders of flow are referred to as azimuthal *anisotropic flow* and are characterized by flow harmonics v_n which are seen as strong collective effects in the QGP. In peripheral heavy-ion collisions, the most dominant higher order flow harmonic is elliptic flow v_2 and arises from the initial almond-like anisotropy of the collision volume given by the *eccentricity* ε_2 (see Figure 2) [38]. The azimuthal distribution seen in Au-Au collisions by the STAR experiment can be seen in Fig. 10a and indicates that the angular particle correlations exhibit elliptic flow, suggesting QGP formation. This anisotropy leads to large pressure gradients in the reaction plane causing an anisotropic momentum distribution. An illustration of some higher orders of flow arising due to fluctuations in the

collision geometry given by ε_n are shown in Fig. 10b. In general, the flow harmonics are proportional to the geometrical fluctuations, $v_n \propto \varepsilon_n$.

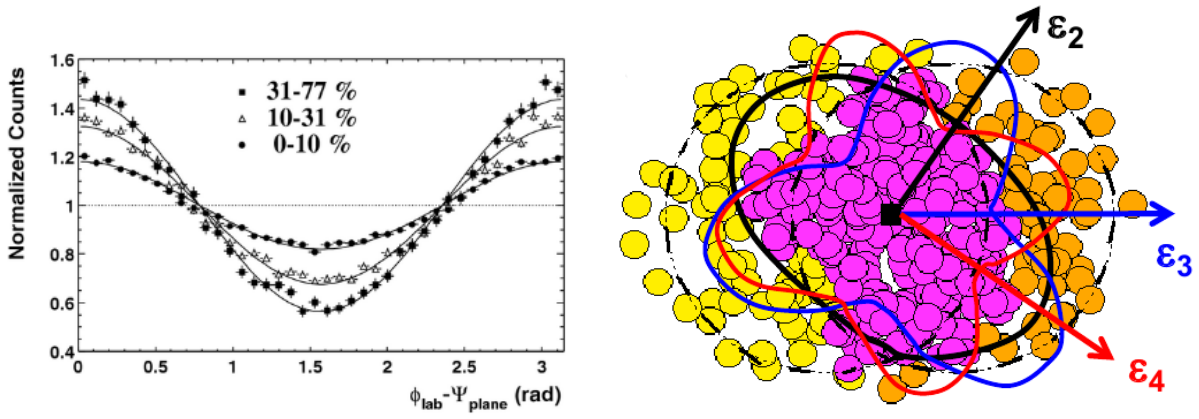

(a) (b)

Figure 10: (a) Azimuthal distribution w.r.t the reaction plane Ψ_{plane} for three collision centrailties from the STAR experiment [39]. The measured v_2 is ~ 0.1 in central collisions (0-10%) and ~ 0.2 in peripheral collisions (31-77%). (b) Illustration of geometrical fluctuations ε_n in the collision volume giving rise to higher order flow harmonics v_n.

The standard procedure for analysing the azimuthal anisotropy is to do a Fourier decomposition which was first introduced by Voloshin and Zhang in 1994 [40]. Previously, flow analysis was done using directivity and sphericity. Now, different orders of flow are characterised by coefficients v_n in the Fourier expansion of the azimuthal dependence of the invariant yield of particles relative to the reaction plane:

$$E\frac{d^3N}{d^3p} = \frac{1}{2\pi}\frac{d^2N}{p_{\text{T}}dp_{\text{T}}dy}[1 + \sum_{n=1}^{\infty} 2v_n \cos(n(\phi - \Psi_{\text{RP}}))]. \tag{9}$$

Here, E is the particle energy, N is the number of particles, p is the particle momentum, n is an integer determining the order of flow, ϕ is the azimuthal angle and Ψ_{RP} is the reaction plane angle which is spanned by the impact parameter and the beamline. Fig. 11a shows a schematic view of a non-central heavy ion collision in the transverse plane. The collision volume is shown in the shaded region with an almond like shape and tilted by an angle given by the reaction plane. The flow parameters v_n are calculated by:

$$v_n = \langle \cos[n(\phi_i - \Psi_{\text{RP}})] \rangle, \tag{10}$$

where the angled brackets indicate an average over all particles in an event. The first flow parameter v_1 is referred to as radial flow and the second parameter v_2 as elliptic flow as already discussed. In general, the flow coefficients are dependent on rapidity and transverse momentum and one refers to them in this context as *differential* flow. Values of v_n that are averaged over regions of transverse momentum or rapidity are called *integrated* flow. Elliptic flow is also a function of the impact parameter which affects the eccentricity of the events and can clearly be seen from Fig. 11a.

Unfortunately, due to the statistical anisotropy of the events, it is not possible to directly calculate the reaction plane angle Ψ_{RP} to determine v_n. However, it can be estimated on an event-by-event basis by using azimuthal correlations between the observed

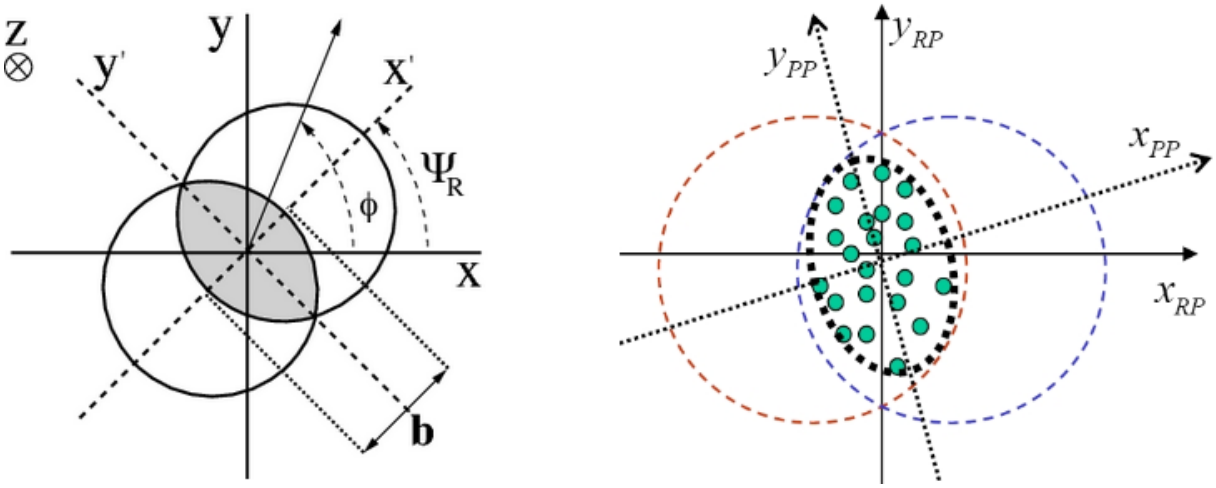

(a) (b)

Figure 11: (a) Schematic of non-central heavy-ion collison, the reaction plane angle is given by Ψ_{R}. (b) The participant plane arising from the participant zone.

particles. Using, for instance, two-particle correlations it is found that

$$\langle \cos(n(\phi_1 - \phi_2)) \rangle = \langle e^{in(\phi_1 - \phi_2)} \rangle = v_2\{2\}^2 = \langle v_n^2 \rangle + \delta_n, \tag{11}$$

where ϕ_1 and ϕ_2 are the azimuthal angles of the two particles. These azimuthal correlations do not only determine anisotropic flow but also two-particle correlations from other sources referred to as *non-flow* which are quantified by the parameter δ_n. These correlations do not necessarily originate from the collective effects of an expanding plasma but rather manifest from the hadronisation and freeze-out phase of the expansion. The dominating non-flow effects are:

- Resonance decay: The angles of the daugther particles from a decayed resonance particle are strongly correlated.
- Particle Jet: Stream of highly correlated particles originating from strong interactions that dominate at high-p_{T}.
- Bose-Einstein correlations: Identical bosons can have highly correlated azimuthal angles.

In general, non-flow effects are due to few-particle correlations and are a source of bias in anisotropic flow measurements. It is suggested that one can suppress the non-flow contribution by using higher order particle correlations, which would minimize the uncertainty in the estimate of the anisotropic flow harmonic. For instance, four-particle correlations are assumed insensitive to non-flow so that $v_2\{4\} \approx \langle v_2 \rangle$.

Anisotropic flow will also fluctuate in direction and magnitude event-by-event, even at fixed centrality. These *flow fluctuations* are described by the variance of the anisotropic flow given by:

$$\sigma_{vn}^2 = \langle v_n^2 \rangle - \langle v_n \rangle^2. \tag{12}$$

The dominant contribution to flow fluctuations originates from the event-by-event fluctuations in the initial collision geometry of the two nuclei defined by the participants

(interacting nucleons). The anisotropy develops in the participant zone spanned by the Participant Plane (PP) and is illustrated in relation to the reaction plane in Fig. 11b. The positions of the participant nucleons will also vary event-by-event which is an important contribution to the flow fluctuations. It is clear that the anisotropy that develops fluctuates due to the eccentricity and the orientation of the major axis. Note that it is necessary to distinguish the flow measured in the reaction plane from that of the participant plane. In general, the flow harmonics in the reaction plane are smaller than in the participant plane ($v_{2,RP} < v_{2,PP}$) and in this thesis the $v_2\{2\}$ and $v_2\{4\}$ observables are measured which estimate the flow seen in the event plane. The N particles in an event are then distributed according to [41]:

$$\frac{dN}{d\phi} \propto f(\phi) = \frac{1}{2\pi}\Big[1 + 2\sum_{n=1}^{\infty} v_n \cos(n(\phi_i - \Psi_n)\Big], \tag{13}$$

where the distribution is now relative to the event plane Ψ_n. The flow harmonics are then in principle calculated from the event plane angle instead (see Eq. 10). From now on the participant plane and the better version of Eq. 9 will always be considered.

3.5 Event Shape Engineering

Event Shape Engineering is a recent method developed by J. Schukraft, A. Timmins and S. Voloshin that makes it possible to select events corresponding to different initial shapes by making use of the strong fluctuations in the initial geometry [10]. Before this method was introduced, the effects of the initial geometry on the final state observables could only be studied by either varying the event centrality or by colliding ions of different shape and size. For instance, the particle dense uranium nuclei are very non-spherical and would provide large initial anisotropies and high multiplicity, making it ideal for anisotropic flow studies. However, there are many possible overlap geometries that have to be classified making the analysis very complex. The ESE method provides a smoother analysis and can study anisotropies even at fixed centrality, making it possible to study the QGP expansion in new ways.

The main principle of the ESE method is to select events based on the magnitude of the reduced flow vector given by:

$$q_n = \frac{|Q_n|}{\sqrt{M}}, \tag{14}$$

where $|Q_n| = \sqrt{Q_{n,x}^2 + Q_{n,y}^2}$ is the magnitude of the n-th order flow vector and M is the multiplicity. The reduced flow vector is defined because the average length of Q_n grows as $\sqrt{M}$ in absence of correlations and works only as a trivial multiplicity dependence. The flow vector components are defined as

$$Q_{n,x} = \sum_{i=1}^{M} \cos(n\phi_i), \quad Q_{n,y} = \sum_{i=1}^{M} \sin(n\phi_i), \tag{15}$$

where ϕ_i is the azimuthal angle of the i-th particle. The average correlation between all particle pairs of an event is related to the magnitude of the q_n vector given by

$$q_n^2 = 1 + (M-1)\langle\cos[n(\phi_i - \phi_j)]\rangle_{i\neq j}. \tag{16}$$

For second order flow, the above equation can be reformulated to show how q_2 depends on the strength of the elliptic flow [42]:

$$\langle q_2^2 \rangle \simeq 1 + \langle (M-1) \rangle \langle (v_2^2 + \delta_2) \rangle, \tag{17}$$

where δ_2 is the non-flow contribution from two-particle correlations. The *mean* v_2 dependence of the q_2 vector is shown in Fig. 12a for Monte Carlo simulated results calculated using 2- and 4-particle correlations at different centrality intervals. The q_2 is calculated in a subevent a while v_2 is calculated in another subevent b, where in this analysis both subevents are statistically independent. In this figure, the *true* values are calculated with no non-flow present, meaning that all correlations in the system are determined by anisotropic flow. When non-flow is introduced it is a significant bias, leading to an overestimation of the flow in high flow events and an underestimation of the flow in low flow events. The aim of this thesis is to study this non-flow bias by using experimental data. The non-flow effects can also be minimized by introducing a rapidity-gap between the two subevents, a useful technique that is further described in Section 5.4.

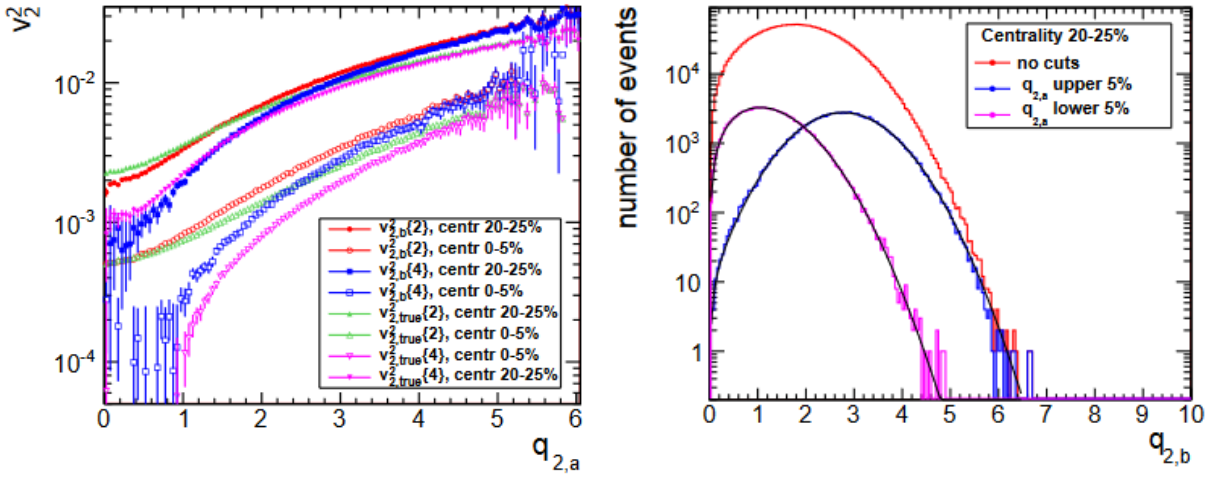

(a) (b)

Figure 12: Behaviour of the q_2-vector in the ESE method [10]. (a) Mean v_2^2 measured in subevent b with 2- and 4-particle cumulants as a function of q_2 measured in subevent a. (b) Distribution of q_2, b with cuts on the corresponding q_2 vector in subevent a.

In practice, the method works by selecting events corresponding to certain intervals of q_2. This is illustrated in Fig. 12b, where the q_2 distribution in subevent b is shown with no cuts and a cut accepting only the events with the 5% highest (lowest) q_2 from subevent a. It can clearly be seen that the cuts introduce an ability to select events with large or small elliptic flow. Since the elliptic flow directly reflects the eccentricity, $v_2 \propto \varepsilon_2$, it suggests then that the flow vector cut is selecting events based on their initial geometry [10]. The average magnitude of the q_2 vector will then also clearly depend on the centrality which means that any analysis is best done in tight centrality intervals.

The ESE technique has already been tested and verified in flow analysis measurements from ALICE and the ATLAS experiment by, for instance, looking at $v_2(p_{\mathrm{T}})$ distributions for several types of identified hadrons and comparing results from ESE selected events to unbiased[6] events [43; 44]. In this thesis, the ESE method is implemented for $v_2(p_{\mathrm{T}})$

[6]In this thesis unbiased events just refers to events with no ESE selection present.

analysis under several different conditions that aims to better understand the effects of fluctuations and non-flow.

4 ALICE - A Large Ion Collider Experiment

The Large Hadron Collider (LHC) is the synchrotron accelerator used for proton and lead-ion collisions at CERN. The LHC consists of two 27 kilometre long, circular, beam pipes held at ultra-high vacuum ($\sim 10^{-10}$ mbar), where ions are accelerated to high energies in opposite directions. The accelerator system and particle detectors are placed approximately 100 metres underground, shielding against outside radiation sources. The main colliding systems are proton-proton (p-p), lead-lead (Pb-Pb) and asymmetric proton-lead (p-Pb) collisions. The maximum design centre-of-mass collision energy in p-p (Pb-Pb) is 14 TeV (5.5 TeV per nucleon) [45]. This large energy is achieved by accelerating the ions to ultra-relativistic speeds using radiofrequency cavities with a strong electric field of about 5 MV/m. The radiofrequency cavities also have a wave-like acceleration effect on the particles causing the beams to split up into bunches. The first heavy ion run at the LHC happened in 2010 and achieved 137 bunches per beam, containing approximately $7 \cdot 10^7$ lead ions each, delivering a peak luminosity of $3 \cdot 10^{25}$ cm^{-2}s^{-1} [46]. The data used in this thesis was obtained from this run and collected at a collision energy of $\sqrt{s_{\mathrm{NN}}} = 2.76$ TeV.

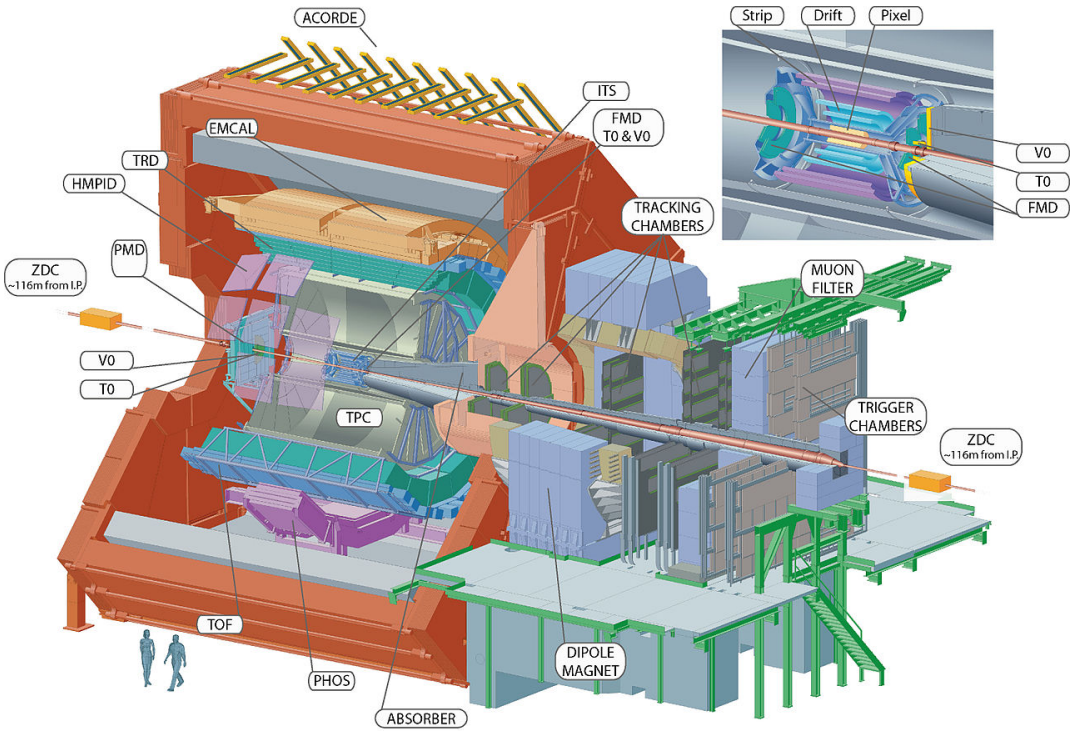

Figure 13: Cut-away of ALICE highlighting the individual detector components [47].

The LHC detector system specifically designed for Pb-Pb collisions is ALICE and is located at one of the eight beam crossing points. ALICE contains a total of 18 sub-detectors, shown in Fig. 13, with the central-barrel detectors (covering full azimuthal angle) embedded in the 0.5 T L3 solenoid magnet [48]. The magnetic field runs parallel to the beam axis, bending the trajectories of charged particles, making it useful for track reconstruction at low-p_{T}. ALICE is required to handle large particle multiplicities in order

to study QGP observables and therefore has excellent particle identification capabilities of charged hadrons in the region $0.15 < p < 20$ GeV/c. This is achieved by detectors with high granularity and tracking sensitivity. The main detectors incorporated in this thesis are the Time Projection Chamber (TPC) and the V0 (or VZERO) detectors, which are presented in the subsequent sections. The Inner Tracking System (ITS), also used in this thesis, lies closest to the collision-point and functions as tracking and vertex finding detectors. The primary collision vertex reconstruction is done using the high granularity Silicon Pixel Detector (SPD).

4.1 The Time Projection Chamber

The Time Projection Chamber (TPC) is an essential detector to ALICE that is able to reconstruct and identify particles in the very high multiplicity environments seen in Pb-Pb collisions. It is able to track particles in three dimensions using particle ionization trajectories. Particle identification is also done using these trajectories and by looking at the ionization energy loss $\mathrm{d}E/\mathrm{d}x$, which is the mean energy deposited per unit length of a charged particle propagating through the gas volume of the TPC. In this thesis, TPC reconstructed tracks from charged particles are used to measure elliptic flow.

The TPC is a 5x5 m hollow cylinder filled with gas that surrounds the inner tracking system. A schematic of the detector design is shown in Fig. 14, where the active volume of the TPC is between 85 to 247 cm with full azimuthal coverage and $|\eta| < 0.9$, making it the biggest TPC in the world [48]. An electric field is created from two endplates towards a central electrode with a high voltage of -100 kV applied. This divides the field cage into two parts and provides an electrostatic field that is uniform along the beam direction and parallel to the magnetic field of the L3 magnet. There are 18 sectors of read-out chambers at the end-caps made out of multi-wire proportional chambers . The detector volume is filled with a $\mathrm{Ne/CO_2/N_2}$ gas mixture.

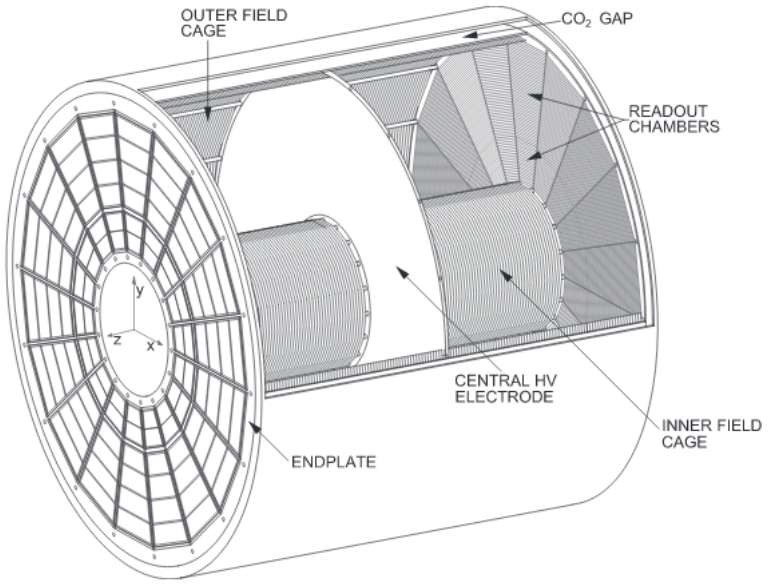

Figure 14: Schematic view of the Time Projection Chamber [49].

When a charged particle propagates through the TPC it will ionize the gas along its trajectory. The emitted electrons will then drift towards the end-plates due to the homogeneous electric field. The information of the drift time allows the z-coordinate of

the corresponding particle to be measured, while r and ϕ are obtain by the endplates. A gating grid prevents electrons from freely drifting to the endplates and a trigger system is used to decide whether to open the gate or not. If an electron is accepted the gate will remain open for ∼90 µs, corresponding to the electron drift time. The accepted electron will experience an electric field that grows as $1/r$ as it moves towards the *anode plane*. The electrons newly acquired energy causes it to further ionize the gas creating an electron avalanche that amplifies the signal. The remaining ions will also drift but in the opposite direction, while inducing a charge on the *cathode plane*. The gate is remained closed for ∼188 µs, to avoid letting the ions drift back into the main TPC volume. The effective dead-time of the TPC is then ∼280 µs, restricting the acceptance to roughly 3600 events per second.

4.2 The V0 Detector

The V0 (or VZERO) detector is located in the forward direction close to the beamline and consists of two detectors called V0A and V0C, which are both ring-segmented scintillator detectors [48]. The V0A detector covers the forward pseudorapidity region ($2.8 < \eta < 5.1$) while V0C covers the backward pseudorapidity region ($-3.7 < \eta < -1.7$). In this thesis the V0C detector is incorporated to broaden the available pseudorapidity coverage used in the elliptic flow analysis. Specifically, it is used for calculating a q_2-distribution that is far away in pseudorapidity from v_2 calculated from TPC reconstructed tracks. The V0 detector is also used for centrality determination, and has a resolution of 0.5-2.0% centrality bin width going from the most central to the very peripheral collisions.

Figure 15a illustrates the layout of the V0 detector compared to the ITS, while Fig. 15b shows how V0A and V0C are segmented. The V0A and V0C are placed at $z = 3.4$ m and $z = -0.9$ from the nominal interaction point. Both detectors are separated in four segments along the radial direction and each ring being further divided in eight sectors in the azimuthal direction. In total, the V0 detector consists of 64 segments which are referred to as *cells* in this thesis. The cell segmentation is quite rough and does not have good angular resolution.

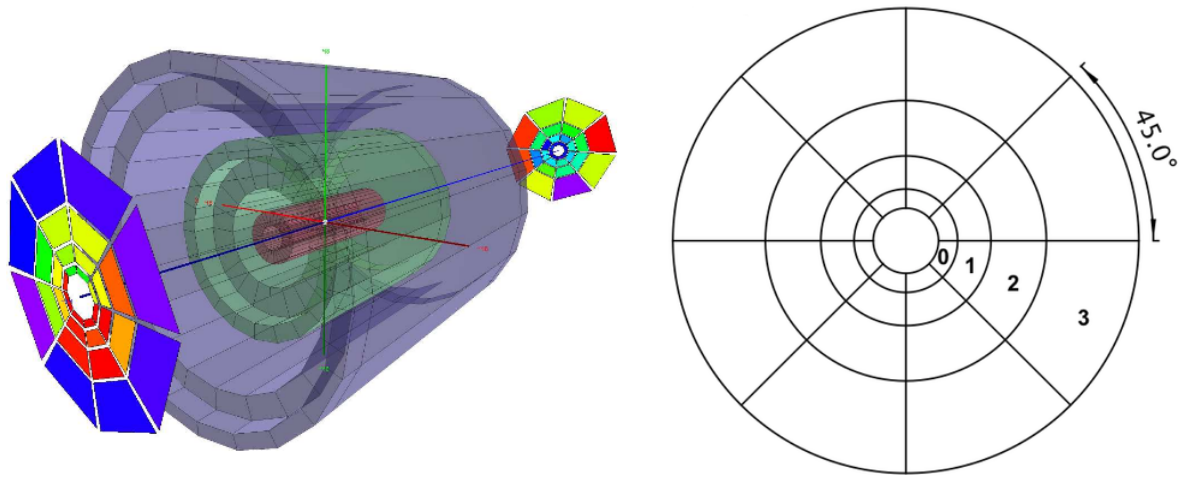

(a) (b)

Figure 15: (a) Illustration of the V0 detector layout in reference to the ITS and (b) V0A and V0C segmentation.

A charged particle that enters the scintillator will lose some energy and in turn ionize

and excite the atoms of the sensitive scintillator material. These atoms will then emit their excess energy in the form of scintillation photons, where the number of photons emitted is proportional to the energy lost by the incoming charged particle. The emitted photons are guided into photomultiplier tubes where a photon has a probability of hitting a photocathode and emitting an electron. The electron is then accelerated towards a series of electrodes, called dynodes, that are held at positive voltages inside the photomultiplier tube. Every time the electron hits a dynode it will knock out a few more electrons which are guided to the next dynode. This causes an electron avalanche that amplifies the signal of the initial photon by a factor around one million before the front-end electronics reads out the signal.

5 Method - Measuring Anisotropic Flow

The standard procedure for measuring anisotropic flow is done by doing a Fourier expansion of the azimuthal dependence of the invariant yield of particles relative to the reaction plane and was already mentioned in Section 3.4.2. This chapter presents the Q-cumulant method [50] used for calculating the flow harmonic v_n for two- and four-particle correlations. In reality, only elliptic flow is calculated in this thesis, however it will be shown that flow vectors for higher order harmonics are needed for the calculations. Therefore, the method is presented unambiguously for arbitrary harmonic which is then trivially applied to elliptic flow ($n = 2$). The chapter then continues with a discussion of how two- and four-particle correlations are affected by fluctuations and non-flow, and ends with a description of the effect of rapidity-gaps when calculating flow.

5.1 Particle Cumulants

For a single event, the average 2- and 4-particle azimuthal correlations are defined as [51]:

$$\langle 2 \rangle = \langle e^{in(\phi_1 - \phi_2)} \rangle = \frac{(M-2)!}{M!} \sum_{i,j=1}^{M} e^{in(\phi_i - \phi_j)}, \ i \neq j, \tag{18}$$

$$\langle 4 \rangle = \langle e^{in(\phi_1 + \phi_2 - \phi_3 - \phi_4)} \rangle = \frac{(M-4)!}{M!} \sum_{i,j,k,l=1}^{M} e^{in(\phi_i + \phi_j - \phi_k - \phi_l)}, \ i \neq j \neq k \neq l, \tag{19}$$

where it is noted that all indices in the sum must be different. Recall that M is the multiplicity. Averaging over all events gives the expression:

$$\langle\langle 2 \rangle\rangle = \langle\langle e^{in(\phi_1 - \phi_2)} \rangle\rangle = \frac{\sum_{\text{events}} (W_{\langle 2 \rangle})_i \langle 2 \rangle_i}{\sum_{\text{events}} (W_{\langle 2 \rangle})_i}, \tag{20}$$

$$\langle\langle 4 \rangle\rangle = \langle\langle e^{in(\phi_1 + \phi_2 - \phi_3 - \phi_4)} \rangle\rangle = \frac{\sum_{\text{events}} (W_{\langle 2 \rangle})_i \langle 4 \rangle_i}{\sum_{\text{events}} (W_{\langle 4 \rangle})_i}, \tag{21}$$

where the double bracket indicates the average first over all particles and then average over all events. The event weights, $W_{\langle 2 \rangle}$ and $W_{\langle 4 \rangle}$, are used to minimize the effect of event-by-event multiplicity fluctuations on the 2- and 4-particle correlations.

The 2- and 4-particle cumulants are estimated by decomposing the azimuthal correlation into its independent contributions and looking at the expectation value of these observables [51]. The cumulants are then determined by:

$$c_n\{2\} = \langle\langle 2\rangle\rangle, \tag{22}$$
$$c_n\{4\} = \langle\langle 4\rangle\rangle - 2 \cdot \langle\langle 2\rangle\rangle^2, \tag{23}$$

where the form given by Borghini *et al.* [52] has been used and is only applicable for detectors with uniform azimuthal acceptance. In the absence of non-flow it can be shown that

$$\langle\langle 2\rangle\rangle = \langle v_n^2\rangle, \tag{24}$$
$$\langle\langle 4\rangle\rangle = \langle v_n^4\rangle, \tag{25}$$

so that different order cumulants give independent estimates to the same reference harmonic v_n, averaged over all events. In the 4-particle cumulant the effects of two-particle correlations are subtracted out of the calculation. The *reference flow* estimated from the 2-particle cumulant and 4-particle cumulant are given by:

$$v_n\{2\} = \sqrt{c_n\{2\}}, \tag{26}$$
$$v_n\{4\} = \sqrt[4]{-c_n\{4\}}, \tag{27}$$

respectively.

5.2 Q-Cumulant Method

The Q-cumulant method [50] for measuring anisotropic flow makes use of the flow vector Q_n, defined as:

$$Q_n = \sum_{i=1}^{M} e^{in\phi_i}, \tag{28}$$

where M is the number of particles. All multi-particle azimuthal correlations can be analytically expressed using Q-vectors of different harmonics. The main advantage of the Q-cumulant method is that it requires only one loop over the data, avoiding the otherwise large computational power needed to calculate all possible particle multiplets when using multi-particle correlations.

The basic principle of the Q-cumulant method is to calculate a reference flow value for 2- and 4-particle cumulants as mentioned in the previous section. The reference flow is calculated for particles over a large region, *e.g.* in transverse momentum or pseudorapidity, and is mainly used to calculate differential flow[7]. The purpose of differential flow is to estimate the 2- and 4-particle cumulants in narrow bins of the observable, so that it can be seen how v_n behaves as a function of said observable. The use of reference flow in the calculation of differential flow provides statistical stability to the calculation, as the narrow bins can contain very few particles.

5.2.1 Two-Particle Reference Flow

The 2-particle correlation given in Eq. 18 can be rewritten in terms of the flow vector Q_n so that

$$Q_n Q_n^* = |Q_n|^2 = \sum_{i,j=1}^{M} e^{in(\phi_i - \phi_j)} = M + \sum_{i,j=1}^{M} e^{in(\phi_i - \phi_j)}, \tag{29}$$

[7]Reference flow is then in principle the same as the integrated flow.

where the last equality of the equation holds when using the restriction $i \neq j$ on the particles. The 2-particle correlation is then given by:

$$\langle 2 \rangle = \frac{|Q_n|^2 - M}{M(M-1)}, \tag{30}$$

which can be solved using a single loop over the data. The next step is then to average this over all events, as shown in Eq. 20. To minimize the multiplicity fluctuations, the event weight is set to be

$$W_{\langle 2 \rangle} = M(M-1), \tag{31}$$

which is just the number of possible ways to combine the particles. This gives us the event average 2-particle cumulant:

$$\langle\langle 2 \rangle\rangle = \frac{\sum_{\text{events}} \langle |Q_n|^2 - M \rangle_i}{\sum_{\text{events}} (M(M-1))_i}, \tag{32}$$

that is just Eq. 20 rewritten. Now, using Eq. 22 for the two particle cumulant and Eq. 26 yields the two-particle reference flow given by:

$$v_n\{2\} = \sqrt{\langle\langle 2 \rangle\rangle}. \tag{33}$$

5.2.2 Four-Particle Reference Flow

The 4-particle reference flow is calculated using the same principles as the 2-particle reference flow, but with generally more complex equations. Similarly as before, the sum in Eq. 19 goes over all particles and can be written in terms of the flow vector as:

$$Q_n Q_n Q_n^* Q_n^* = |Q_n|^4 = \sum_{i,j,k,l=1}^{M} e^{in(\phi_i + \phi_j - \phi_k - \phi_l)}. \tag{34}$$

Now, requiring that all the particles are different, *i.e.* $i \neq j \neq k \neq l$, is not a trivial step, but it can be shown analytically [50] that

$$\langle 4 \rangle = \frac{|Q_n|^4 + |Q_{2n}|^2 - 2 \cdot \Re[Q_{2n} Q_n^* Q_n^*]}{M(M-1)(M-2)(M-3)} - 2\frac{2(M-2) \cdot |Q_n|^2 - M(M-3)}{M(M-1)(M-2)(M-3)}, \tag{35}$$

where $\Re$ indicates the real part of the argument. Again, the event weight is chosen to be:

$$W_{\langle 4 \rangle} = M(M-1)(M-2)(M-3), \tag{36}$$

to minimize the event-by-event multiplicity fluctuations. Calculating the event average 4-particle cumulant and using Eq. 23 and Eq. 27 gives the four-particle reference flow:

$$v_n\{4\} = \sqrt[4]{-(\langle\langle 4 \rangle\rangle - 2 \cdot \langle\langle 2 \rangle\rangle^2)}. \tag{37}$$

A source of bias can arise when calculating the four-particle correlations which originates from the fact that the number of particle associations grows approximately as M^4. Therefore, there is a possibility that the measured v_2 is biased towards the subsample with abnormally large multiplicity deviation, far from the mean of the measured events. The effect of this on the elliptic flow measurement is shown in Section 6.5.

5.2.3 Differential Flow

The differential flow is calculated in narrow bins and makes use of the initial reference flow measurement to provide stability, as mentioned in Section 5.2. It is now necessary to keep track of which particles are used for the reference flow measurement and/or the differential flow measurement. The particles used for the reference flow measurement are labeled as Reference Particles (RP), of which there are M in total in each event. The particles used in determining differential flow are labeled as Particles of Interest (PoI) with m_p of them in each event. Finally, it is possible that the RP and PoI have an overlap, so that a particle can be labeled as RP and PoI simultaneously. There are m_q of these particles.

5.2.4 Two-Particle Differential Flow

The two-particle azimuthal correlator, also called the reduced two-particle correlator, is defined as:

$$\langle 2' \rangle = \langle e^{in(\psi_1 - \phi_2)} \rangle = \frac{1}{m_p M - m_q} \sum_{i=1}^{m_p} \sum_{j=1}^{M} e^{in(\psi_i - \phi_j)}, \ i \neq j, \tag{38}$$

where ψ_i is the azimuthal angle of the i-th particle of interest (PoI). Note again, that the indices i and j must be taken different. To simplify this calculation, and also the four-particle azimuthal correlator calculation in the next section, the following vectors are introduced:

$$p_n = \sum_{i=1}^{m_p} e^{in(\psi_i)}, \tag{39}$$

$$q_n = \sum_{i=1}^{m_q} e^{in(\psi_i)}, \tag{40}$$

where p_n is summed over all PoI and q_n is summed over all PoI that are also reference particles (RP). It can then be shown that the reduced two-particle correlator can be written as [50]:

$$\langle 2' \rangle = \frac{p_n Q_n^* - m_q}{m_p M - m_q}, \tag{41}$$

and, averaged over all events, the expression becomes:

$$\langle\langle 2' \rangle\rangle = \frac{\sum_{\text{events}} (W_{\langle 2' \rangle})_i \langle 2' \rangle_i}{\sum_{\text{events}} (W_{\langle 2' \rangle})_i}. \tag{42}$$

Using the same arguments of minimizing the multiplicity fluctuations, the event weight is defined as:

$$W_{\langle 2' \rangle} = m_p M - m_q. \tag{43}$$

Similar to the approach used before, the two-particle differential cumulant is given by

$$d_n\{2\} = \langle\langle 2' \rangle\rangle. \tag{44}$$

Finally, the estimate of differential flow v_n' for two-particle cumulants is

$$v_n'\{2\} = \frac{d_n\{2\}}{\sqrt{c_n\{2\}}}, \tag{45}$$

as described by Bilandzic *et al.* [50]. In the final expression, assuming no flow fluctuations, we have that $d_n\{2\} = \langle v_n' v_n \rangle$, where v_n' is the differential flow and v_n is the reference flow. The denominator is given by $c_n\{2\} = \langle v_n^2 \rangle$, so that the overall reference flow harmonic v_n drops out from Eq. 45. Therefore, it is clear that reference flow, with its large particle statistics, only provides statistical stability to both the numerator and denominator in the above equation.

5.2.5 Four-Particle Differential Flow

Making use of the p- and q-vectors defined in the previous section one can, correspondingly, define the reduced four-particle correlator as:

$$\begin{aligned}\langle 4' \rangle = \Big[& p_n Q_n Q_n^* Q_n^* - q_{2n} Q_n^* Q_n^* - p_n Q_n Q_{2n}^* - 2 \cdot M p_n Q_n^* - 2 \cdot m_q |Q_n|^2 \\ & + 7 \cdot q_n Q_n^* - Q_n q_n^* + q_{2n} Q_{2n}^* + 2 \cdot p_n Q_n^* + 2 \cdot m_q M - 6 \cdot m_q \Big] \\ & \Big/ \Big[(m_p M - 3 m_q)(M-1)(M-2) \Big]. \end{aligned} \tag{46}$$

Taking the average over all events gives

$$\langle\langle 4' \rangle\rangle = \frac{\sum_{\text{events}} (W_{\langle 4' \rangle})_i \langle 4' \rangle_i}{\sum_{\text{events}} (W_{\langle 4' \rangle})_i}, \tag{47}$$

where the event weight is defined as:

$$W_{\langle 4' \rangle} = (m_p M - 3 m_q)(M-1)(M-2). \tag{48}$$

The fourth order differential cumulant is then given by [50]:

$$d_n\{2\} = \langle\langle 4' \rangle\rangle - 2 \cdot \langle\langle 2' \rangle\rangle \langle\langle 2 \rangle\rangle. \tag{49}$$

The final four-particle differential cumulant is

$$v_n'\{4\} = -\frac{d_n\{4\}}{(-c_n\{4\})^{3/4}}. \tag{50}$$

5.3 Fluctuations and Non-Flow Effects

The particle cumulants are known to be affected by flow fluctuations [9] and was previously discussed in Section 3.4.2. The reference flow measured with two- and four-particle cumulants are estimated as:

$$\begin{aligned} v_n\{2\} &= \langle v_n^2 \rangle^{1/2} \approx \langle v_n \rangle + \frac{1}{2} \frac{\sigma_{v_n}^2}{\langle v_n \rangle}, \\ v_n\{4\} &= (-\langle v_n^4 \rangle + 2 \langle v_n^2 \rangle^2)^{1/4} \approx \langle v_n \rangle - \frac{1}{2} \frac{\sigma_{v_n}^2}{\langle v_n \rangle}, \end{aligned} \tag{51}$$

where $v_2\{2\}$ is being enhanced by the flow fluctuations and $v_2\{4\}$ is being suppressed by an equal amount. Recall that $\langle v_n \rangle$ is the mean value of the flow coefficient and that the flow fluctuations are characterized by $\sigma^2_{v_n}$ as described in Eq. 12. The approximation done in the above equation assumes that the fluctuations are much smaller than the mean flow value. The fluctuations in the situation where a differential flow is obtained using the reference flow are more complicated and will not be discussed here (see *e.g.* A. Colliander Hansen [53]).

The particle cumulants are also subject to bias from non-flow. Contributions of two-particle correlations grow as $\delta_2 \propto 1/M$, whereas four-particle non-flow correlations scale as $\delta_4 \propto 1/M^3$. Therefore, the effects of non-flow on four-particle correlations are almost negligible, although they are subject to phenomena such as particle jets. In an ideal case where non-flow is only present in two-particle correlations it can be shown that the four-particle cumulant $c_2\{4\}$ completely removes this effect [54].

By assuming that $\sigma_{v_2}^2$ and δ_2 are to leading order additive quantities it is found that

$$v_2\{2\}^2 = \langle v_2^2 \rangle + \delta_2 + \sigma^2_{v_2}, \quad v_2\{4\}^2 = \langle v_2^2 \rangle - \sigma^2_{v_2}. \tag{52}$$

The difference between these estimates leads to interesting observables of fluctuation and non-flow effects. In particular, the quantities $v_2\{2\} - v_2\{4\}$ and $v_2\{2\}^2 - v_2\{4\}^2$ are measured in this thesis under the assumption that the ESE technique can remove the fluctuations due to the event-by-event anisotropies. The differences are then given by:

$$\begin{aligned} v_2\{2\} - v_2\{4\} &\approx \delta_2 + \frac{\sigma^2_{v_n}}{\langle v_n \rangle} \xrightarrow[ESE-selection]{} \delta_2, \\ v_2\{2\}^2 - v_2\{4\}^2 &\approx \delta_2 + 2\sigma^2_{v_n} \xrightarrow[ESE-selection]{} \delta_2. \end{aligned} \tag{53}$$

5.4 Rapidity-Gaps

It was mentioned in the previous section that two-particle cumulants (and four-particle cumulants to some extent) are subject to bias from non-flow correlations. By introducing a rapidity-gap in between the flow-vectors it is possible to reduce these few-particle correlations. The idea is that if a rapidity gap $\Delta\eta$ is larger than the pseudorapidity interval between two non-flow correlated particles, then this correlation will not contribute to the flow measurement. The two-particle differential flow given by Eq. 45 can then be written as:

$$v'_n\{2, |\Delta\eta| > x\} = \frac{\langle v'_n v_{n,C} \rangle}{\sqrt{\langle v_{n,A} v_{n,B} \rangle}}, \tag{54}$$

where x is the minimum separation in pseudorapidity $\Delta\eta$. The notations A and B refer to calculations of the reference flow in two different rapidity regions. There is also a rapidity gap between the differential flow and the reference flow calculated in region C. The extraction of $\langle v'_n \rangle$, ignoring flow fluctuations, is done by requiring that $v_{n,A} = v_{n,B} = v_{n,C}$ so that we find

$$v'_n\{2, |\Delta\eta| > x\} = \frac{\langle v'_n v_n \rangle}{\sqrt{\langle v_n^2 \rangle}} = \langle v'_n \rangle. \tag{55}$$

Introducing a rapidity-gap will not change the calculation of the differential cumulant $d_n\{2\}$ in Eq. 44, however it implies that $m_q = 0$, as there is no overlap between RP and PoI.

6 Analysis Method - Selecting the Right Events

This chapter presents a detailed description of the selection criteria implemented for the elliptic flow analysis. First, the data taking details for the event selections with the ALICE detector are shown, followed by the q_2 cuts implemented with the ESE technique. A discussion of the V0 calibration and implementation for flow analysis as well as a preliminary investigation of $v_2\{2\}$ and $v_2\{4\}$ calculations are also presented.

The data processing and event analysis is done using a standard particle and heavy ion physics software called `ROOT` [55]. The software is an object oriented framework written in `C++` with a built in `C++` interpreter and is specifically made for large scale data analysis. `ROOT` is equipped with many functions allowing for advanced statistical analysis and visualisation tools. Interacting with the software was done via a graphical user interface, the command line and the text editor `Emacs` [56].

6.1 Data and Event Selections

The elliptic flow analysis is performed using data recorded by the ALICE detector[8] from Pb-Pb collisions at $\sqrt{s_{\mathrm{NN}}} = 2.76$ TeV. The data consists of runs where the TPC and ITS both have good performance. Pile-up events containing multiple Pb-Pb collisions are removed by requiring that the primary vertex reconstructed with the SPD lies within 0.5 cm along the beamaxis of the primary vertex reconstructed using tracks ($|vtx_z - vtx_z^{SPD}| < 0.5$ cm). Also, events are required to have a primary vertex position that lies within 10 cm of the apparent interaction point in the beam direction ($|vtx_z| < 10$ cm) and within 0.3 cm in the transverse plane ($|vtx_{x,y}| < 0.3$ cm). The event centrality is estimated using the multiplicity (signal) distribution from the V0 detector. In total there are $\sim 11.98 \cdot 10^6$ events available for analysis.

Further event selections are done to optimize the elliptic flow analysis. The reference flow is calculated in the transverse momentum interval $0.5 < p_{\mathrm{T}} < 5$ GeV/c, where the lower boundary is due to the deteriorating tracking capabilities of the ALICE detector that occurs around $\sim$0.2 GeV/c. The upper limit is set at 5 GeV/c and is due to the fact that the high-p_{T} spectra are dominated by particle jets. These are highly correlated particles that contribute to the non-flow bias in the analysis. In general, the elliptic flow measurement is also restricted to the pseudorapidity range $|\eta| < 0.8$, and is due to the limited acceptance range of the TPC and the requirement for uniform azimuthal acceptance. Finally, only *charged* particles are considered for this analysis.

6.2 Event Shape Engineering Selections

The ESE technique is implemented for the elliptic flow measurement by introducing selections on the second-order reduced flow vector q_2, as described in Section 3.5. The analysis is further restricted in centrality to accept events that fall in the narrow interval $35-40\%$. This is done to ensure an approximately flat centrality dependence of the average q_2 distribution. The narrow centrality interval is also chosen in a region where collisions are peripheral while still maintaining high multiplicity events. In this region the elliptic flow is maximal and the high multiplicity ensures good statistics.

The elliptic flow analysis performed in this thesis implements q_2-selections for three different cases. In each case, either the elliptic flow observable or the q_2 observable is

[8] Specifically the LHC10h dataset.

measured in different pseudorapidity intervals, while still maintaining the cuts previously mentioned. The observables $v_2\{2\} - v_2\{4\}$ and $v_2\{2\}^2 - v_2\{4\}^2$ mentioned in Section 5.3 are of particular interest for judging the effects of non-flow and fluctuations in different situations. The three cases are described as follows:

- **η-separation between v_2 and q_2:** The elliptic flow from two- and four-particle correlations is measured using TPC reconstructed tracks in the pseudorapidity window: $|\eta| < 0.8$. The q_2-distribution is constructed using the signal amplitude in the V0 detector and is defined as q_2^{V0C}. This ensures a separation on more than one unit in pseudorapidity between $v_2\{2\}$ ($v_2\{4\}$) and q_2^{V0C}, which has the effect of suppressing non-flow contributions. This large pseudorapidity separation makes it possible to assess the bias from non-flow correlations. The large TPC coverage at mid-rapidity ensures high multiplicity in the elliptic flow calculation.

- **v_2 rapidity-gap and η-separated q_2:** The calculation of $v_2\{2\}$ ($v_2\{4\}$) is done in the pseudorapidity interval $0.4 < |\eta| < 0.8$, creating a rapidity-gap (as described in Section 5.4) with a large separation of $|\Delta\eta| \geqslant 0.8$. This suppresses the non-flow contribution in the calculation of $v_2\{2\}$ and $v_2\{4\}$. The q_2 distribution is calculated in the pseudorapidity window $|\eta| < 0.4$ and is defined as $q_2^{\mathrm{TPC}}\{|\eta| < 0.4\}$. This selection is compared to the q_2^{V0C} selection to assess the flow selectivity. However, this method will lack statistics due to only using half the TPC data.

- **Full TPC calculation of v_2 and q_2:** A *raw* calculation of $v_2\{2\}$ ($v_2\{4\}$) and q_2 is done in the pseudorapidity interval $|\eta| < 0.8$ for TPC reconstructed tracks, where the definition q_2^{TPC} is made for the second-order reduced flow vector. It is expected that there are strong correlations between the observables v_2 and q_2. The large multiplicity at mid-rapidity and the good resolution of the TPC maximizes the discriminating power of q_2, allowing for good event shape selection.

The distributions of the second-order reduced flow vectors for the above cases are shown in Fig. 16. The size of the distributions is related to how large the pseudorapidity coverages are in the different selections. The q_2^{V0C} is largest since the V0C detector covers a larger pseudorapidity window, meaning it integrates a larger multiplicity. Similarly, it is seen that $q_2^{\mathrm{TPC}} > q_2^{\mathrm{TPC}}\{|\eta| < 0.4\}$ due to having a larger multiplicity integration. The blue (red) vertical line in the diagrams indicate the selection of events with the bottom (top) 10% q_2. These selections are done in narrow intervals of 10% over the q_2-distributions, ensuring that events with very similar initial geometry are selected. The event shape selectivity are related to the magnitude of elliptic flow where the detector is located as well as on the available multiplicity and detector performance. The TPC detector has good resolution and covers the central rapidity region where elliptic flow is large. The V0C detector, however, is located at backward rapidity and has poor resolution (limited azimuthal segmentation). Therefore, it is expected that the TPC q_2-distributions provide the best event shape selectivity.

The method for calculating a percentile of events based on the magnitude of the q_2-vector is done in the following way[9]: First the q_2-distribution is normalized. Then, the `ROOT` function `GetIntegral()` is implemented, returning a pointer to the array of bins integral. A `TGraph` is used to plot the un-normalized q_2-distribution against the integral bins. Evaluating the graph at any value from zero to one returns the corresponding q_2-value so that any percentile selection of the q_2-distribution can be made.

[9]The author would like to thank Vytautas Vislavicius for presenting this method.

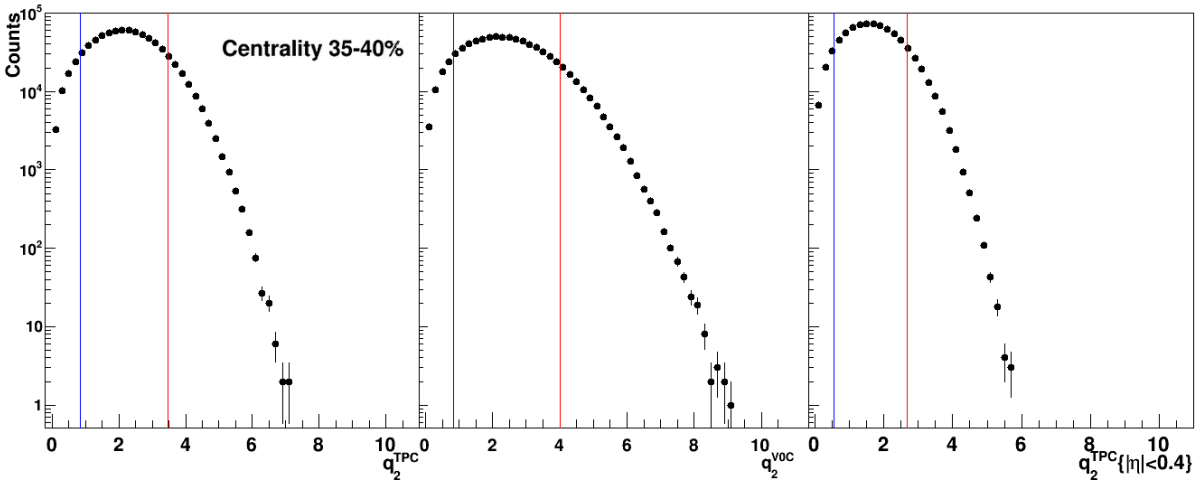

Figure 16: The q_2-distributions for the full TPC (left), the V0C (middle) and the partial TPC (right) .

6.3 Calibrating the V0 Detector for Flow Analysis

To be able to use the V0C detector for flow analysis one first needs to calibrate it. This is necessary because the gains on the 64 V0 cells are set individually. As a consequence, two different cells with the same ADC counts do not correspond to the same amount of particle hits. To be able to construct the flow vector in the V0 detector, all the channels need comparable ADC values. The calibration approach is then to associate each channel i with an equalization factor $f_{\text{eq,i}}$. To calculate this factor one makes use of the raw ADC counts shown in Fig. 17a, where the first 32 cells correspond to the V0C detector and the next 32 cells correspond to the V0A detector. Note that the ADC counts are directly proportional to the multiplicity. That is, a large signal amplitude indicates a large multiplicity. From the raw ADC spectra one calculates the mean value over all the cells ADC_{mean}. The next step is then to calculate the mean ADC value over each individual V0 cell given by $\text{ADC}_{\text{mean},i}$. Note that this mean is over all the events used in the data analysis. The equalization factor is then given by:

$$f_{\text{eq,i}} = \frac{\text{ADC}_{\text{mean},i}}{\text{ADC}_{\text{mean}}}. \tag{56}$$

The calculated equalization factors are shown in Appendix A. Dividing the raw ADC amplitude with the respective cell's equalization factor produces the calibrated V0 amplitude spectra, shown in Fig 17b. In general, the signal amplitudes are uniform within 10-20% [34].

6.4 V0C Second-Order Reduced Flow Vector Calculation

The V0C is divided into eight sectors of 45° each, providing granularity in the azimuthal plane. To use the information of the calibrated V0 detector for calculating the reduced flow vector q_2, the azimuthal angle of the center corresponding to each sector is needed. Recall that the V0C detector is located in the backward rapidity-region and is also segmented into four rings along the radial direction. The azimuthal angle of the center of the sector

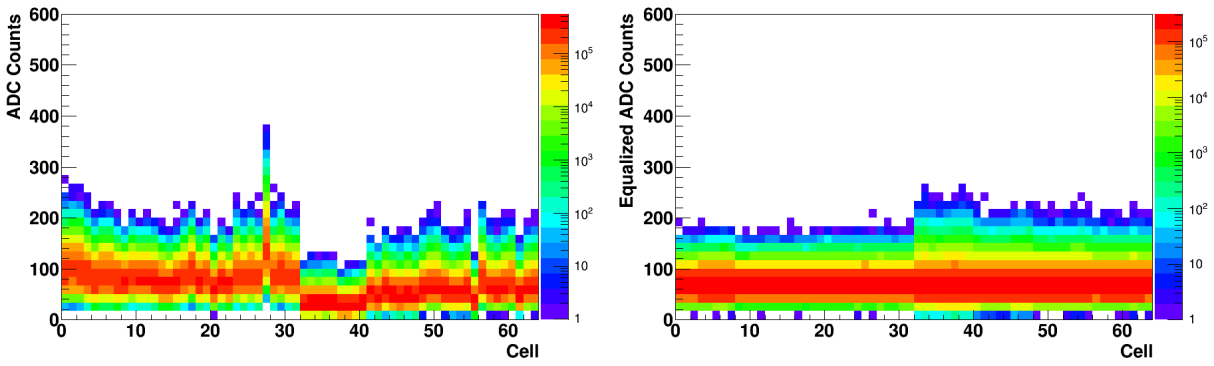

(a) (b)

Figure 17: (a) The raw ADC counts in the V0 detector. (b) Equalized ADC counts in the V0 detector. The color-bar indicates the amplitude distribution for all analysed events.

that includes cell i is then given by[10]:

$$\phi_i = \frac{\pi}{4}(0.5 + i \bmod 8), \tag{57}$$

where i mod 8 gives the remainder of cell i divided by 8 using the modulus operator.

The implementation of the V0C for flow analysis works under the assumption that the detector has uniform azimuthal acceptance. Recall that the second-order reduced flow vector is given by:

$$q_2 = \frac{|Q_2|}{\sqrt{M}}, \tag{58}$$

where $|Q_2| = \sqrt{Q_{2,x}^2 + Q_{2,y}^2}$ is the magnitude of the second-order flow vector and M is the multiplicity. Knowing the azimuthal angles ϕ_i, the reduced flow vector components are given by $Q_{2,x} = \sum_{i=1}^{32} w_i \cos 2\phi_i$ and $Q_{2,y} = \sum_{i=1}^{32} w_i \sin 2\phi_i$ with $M = \sum_{i=1}^{32} w_i$. The sum runs over the 32 cells in the V0C detector and w_i is the measured amplitude in cell i. The V0C multiplicity M is directly proportional to the signal strength and is therefore estimated as the sum of the amplitudes measured in each channel.

6.5 Preliminary Measurement and Investigation of Elliptic Flow

Before doing the Event Shape Engineering analysis, a short preliminary measurement of v_2 using the Q-cumulant method was done to validate the analysis performed in this thesis. The transverse momentum distributions of $v_2\{2\}$ and $v_2\{4\}$ are presented in Fig. 18 using charged particles selected in the $40-50\%$ centrality interval with $|\eta| < 0.8$. The measured elliptic flow is compared to published ALICE results for charged particles with the same centrality and collision energy [57]. The measurement shows good agreement with the ALICE results and indicates a saturation of elliptic flow occurring around 3 GeV/c. The ALICE results suffer from low statistics due to using fewer events in the analysis which can be clearly seen from the statistical error-bars. The v_2 measured here can easily be extended to high-p_{T} regions without overwhelming statistical errors. Another source of

[10]The author would like to thank Martin Ljunggren for showing how the azimuthal angle in the V0C is calculated.

uncertainty is the multiplicity in the events, which is directly related to the centrality of the event. To maximize v_2 and minimize the uncertainty one needs to select events with peripheral collisions and large multiplicity. Centrality intervals that fulfill these conditions lie in the range $\sim(20-50)\%$.

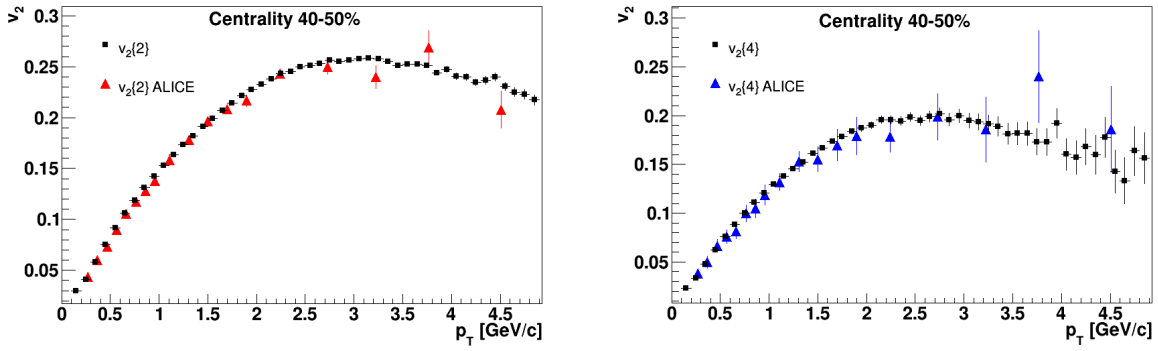

(a) (b)

Figure 18: (a) Measured elliptic flow using two-particle correlations and (b) four-particle correlations. A comparison to ALICE results is also shown [57].

It was mentioned in Section 5.2.2 that $v_2\{4\}$ can be significantly biased by high multiplicity events. To see the effects of this one can introduce a multiplicity cut in the event selection. Fig. 19a shows the multiplicity distribution of events in the 40-50% centrality interval. The same elliptic flow measurement was performed but accepting only events with a multiplicity of $M < 1000$. The ratio between the multiplicity selected and unbiased measurements is shown in Fig. 19b and indicates a deviation of approximately 1%. This small effect is likely due to a lack of high multiplicity events seen in the data. The multiplicity cut was therefore left out of the elliptic flow studies presented in this thesis. However, it could prove to be of noticeable impact in data with many large multiplicity events that deviate far from the mean multiplicity.

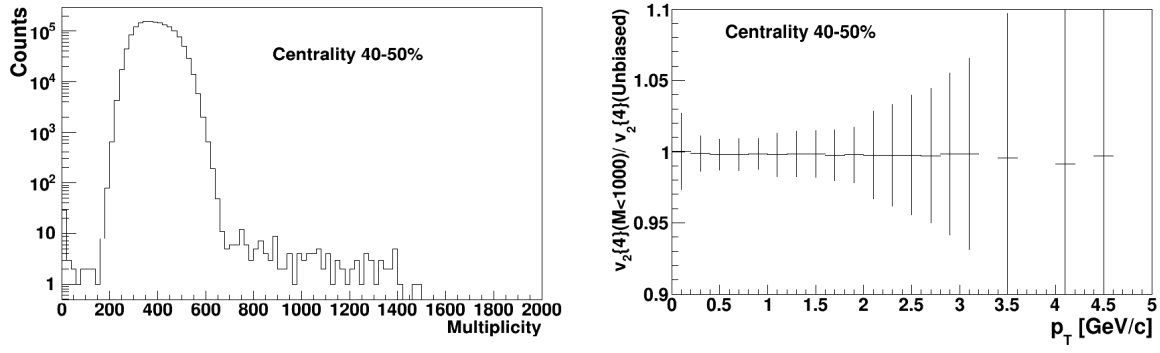

(a) (b)

Figure 19: (a) Unbiased multiplicity distribution and (b) ratio between unbiased and multiplicity selected four-particle elliptic flow.

7 Results

The Q-cumulant method for calculating the transverse momentum dependence of the elliptic flow harmonic v_2 using two- and four-particle correlations was presented in Section 5.2. The calculations use a reference flow in the interval $0.5 < p_{\mathrm{T}} < 5$ GeV/c. There was also a discussion on how $v_2\{2\}$ and $v_2\{4\}$ are biased by fluctuations, enhancing and suppressing the measured elliptic flow respectively. The non-flow bias leads to an overestimate of the measured elliptic flow.

This thesis presents elliptic flow measurements of $v_2\{2\}(p_{\mathrm{T}})$ and $v_2\{4\}(p_{\mathrm{T}})$ using the discriminating power of the second-order reduced flow vector q_2 presented with the Event Shape Engineering technique (see Section 3.5). This makes it possible to select events where the initial eccentricity of the collision volume is very similar causing the geometry flow fluctuations to be suppressed. Looking at the difference between $v_2\{2\}$ and $v_2\{4\}$ under these conditions are done to provide insight into non-flow behaviour.

The results are achieved for three situations according to the event selections in Section 6.2. First, the transverse momentum distributions are presented. Then the chapter ends with result of the first and second order differences between $v_2\{2\}$ and $v_2\{4\}$.

7.1 Transverse Momentum Distributions

The charged particle elliptic flow using two- and four-particle correlations as a function of transverse momentum for 35-40% centralities from $\sqrt{s_{\mathrm{NN}}} = 2.76$ TeV Pb-Pb collisions at ALICE is shown in Fig. 20. The $v_2\{2\}$ and $v_2\{4\}$ measurements are done using reconstructed tracks in the TPC pseudorapidity interval $|\eta| < 0.8$, and also for $0.4 < |\eta| < 0.8$ creating a rapidity-gap of $|\Delta\eta| \geqslant 0.8$. The separation seen between $v_2\{2\}$ and $v_2\{4\}$ is a consequence of their opposite-sign fluctuation bias.

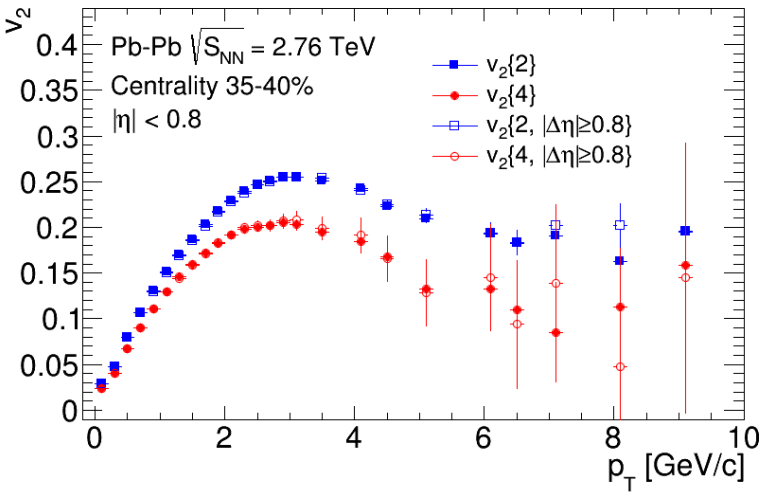

Figure 20: Measured elliptic flow using two-particle correlations (blue) and four-particle correlations (red) for 35-40% centralities. Results from elliptic flow measurements with a rapidity-gap of at least 0.8 units are also shown as open squares and circles.

Figure 21a and 21b shows how the measured $v_2\{2\}$ and $v_2\{4\}$ from q_2^{V0C}-selected events compare to the event shape unbiased measurement for 35-40% centralities. The ESE selections are done by accepting the events with the top 10% largest q_2^{V0C} and the events

with the bottom 10% q_2^{V0C}. The V0C q_2-distribution was shown in Section 6.2. The unbiased elliptic flow measurement corresponds to no ESE-discrimination present in the event selection. The subplots show the ratios $v_2\{2\}$(ESE-selected)/$v_2\{2\}$(Unbiased) and $v_2\{4\}$(ESE-Selected)/$v_2\{4\}$(Unbiased) for $v_2\{2\}$ and $v_2\{4\}$, respectively. Corresponding results are also shown in Fig. 22 and 23 for $q_2^{\mathrm{TPC}}\{|\eta| < 0.4\}$-selected events and q_2^{TPC}-selected events, respectively. Note that the scaling of the ratios in Fig. 23 are different to highlight the effects seen in the q_2^{TPC}-selection, where the bottom 10% events for $v_2\{2\}$ become negative. The etagap study (Fig. 22) have the largest statistical errors due to only using approximately half the available data. It is clearly seen that the V0C provides the weakest event shape selection while the full TPC analysis provides the largest elliptic flow deviation from the unbiased measurements.

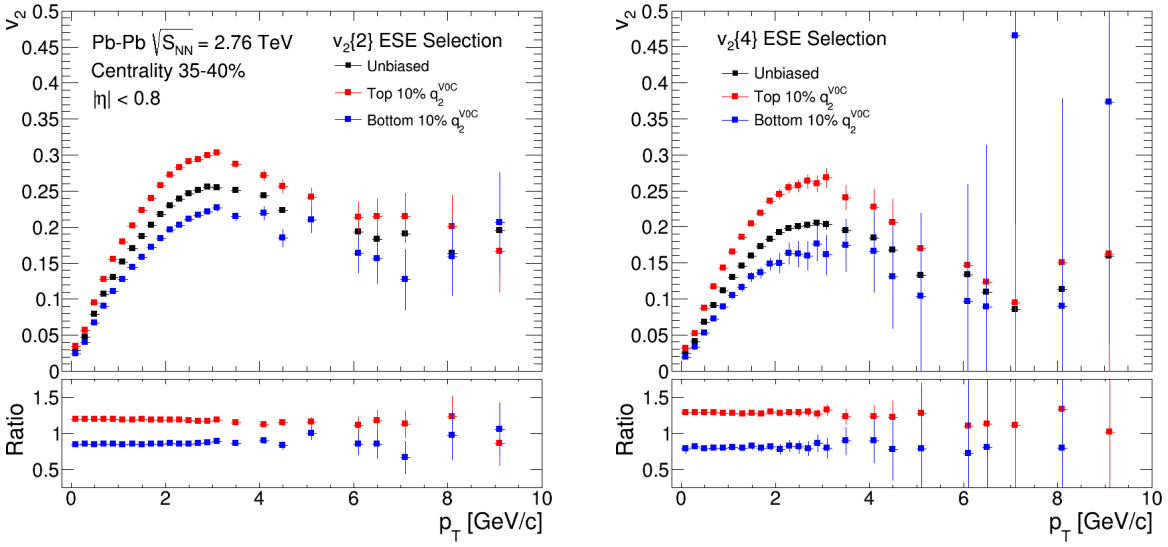

(a) (b)

Figure 21: Measured elliptic flow transverse momentum distribution using (a) two-particle correlations and (b) four-particle correlations for top (bottom) 10% q_2^{V0C}-selected and unbiased events. The ratio of ESE-selected to unbiased elliptic flow is also shown.

Direct comparisons between the measured $v_2\{2\}$ and $v_2\{4\}$ in q_2^{V0C}-selected events are shown in Fig. 24. Intermediate q_2^{V0C}-intervals going from the bottom 10% to the top 10% are shown and highlights the selectivity of the q_2^{V0C}-vector. The size of the elliptic flow is approximately 20% larger in the top 10% events compared to the bottom 10% events. The same event shape evolution is shown in Fig. 25 and Fig. 26 for $q_2^{\mathrm{TPC}}\{|\eta| < 0.4\}$-selected and q_2^{TPC}-selected events, respectively. It is clear that calculating the q_2-distributions in the TPC provide much better event shape discrimination than the V0C as the measured elliptic flow at intermediate p_{T} is approximately a factor 2 greater for $q_2^{\mathrm{TPC}}\{|\eta| < 0.4\}$ and a factor $\sim$2.7 greater for q_2^{TPC}. The two- and four-particle correlations are seen to almost overlap for elliptic event shapes in the full TPC study, suggesting that the flow fluctuations have been removed. Signs of reduced fluctuations are also seen when using $q_2^{\mathrm{TPC}}\{|\eta| < 0.4\}$ and q_2^{V0C} to select the event shape (compared with Fig. 20).

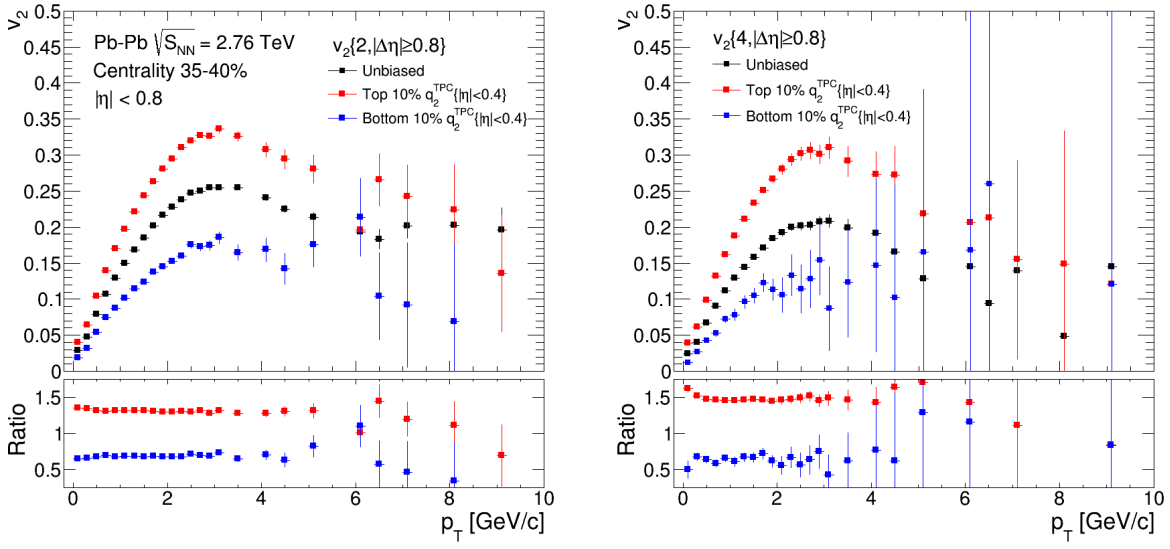

(a) (b)

Figure 22: Measured transverse momentum distribution of $v_2\{\ ,|\Delta\eta| \geqslant 0.8\}$ using (a) two-particle correlations and (b) four-particle correlations for top (bottom) 10% $q_2^{\mathrm{TPC}}\{|\eta| < 0.4\}$-selected and unbiased events. The ratio of ESE-selected to unbiased elliptic flow is also shown.

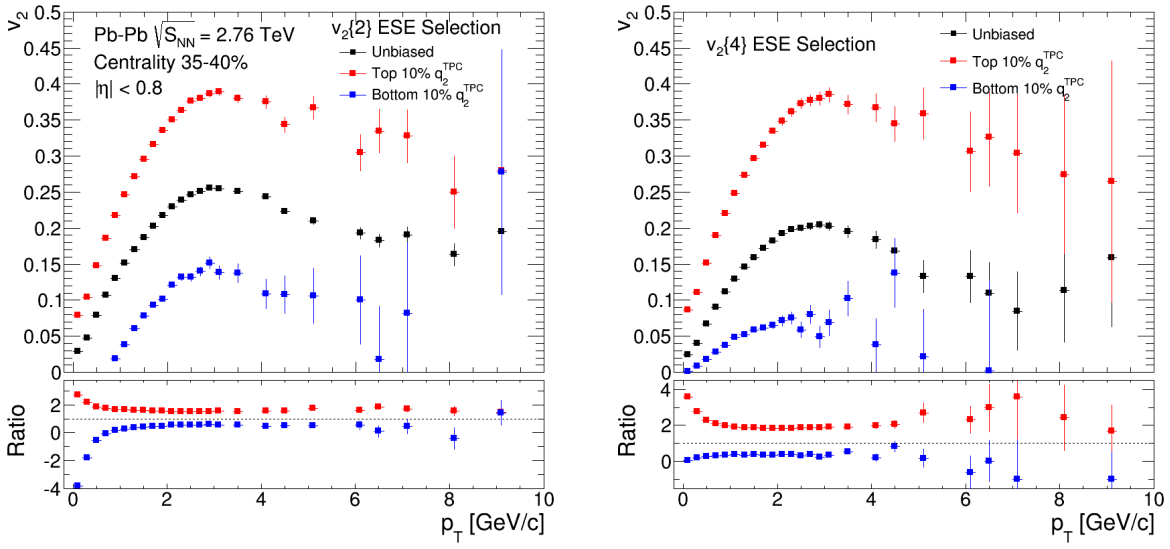

(a) (b)

Figure 23: Measured elliptic flow transverse momentum distribution using (a) two-particle correlations and (b) four-particle correlations for top (bottom) 10% q_2^{TPC}-selected and unbiased events. The ratio of ESE-selected to unbiased elliptic flow is also shown.

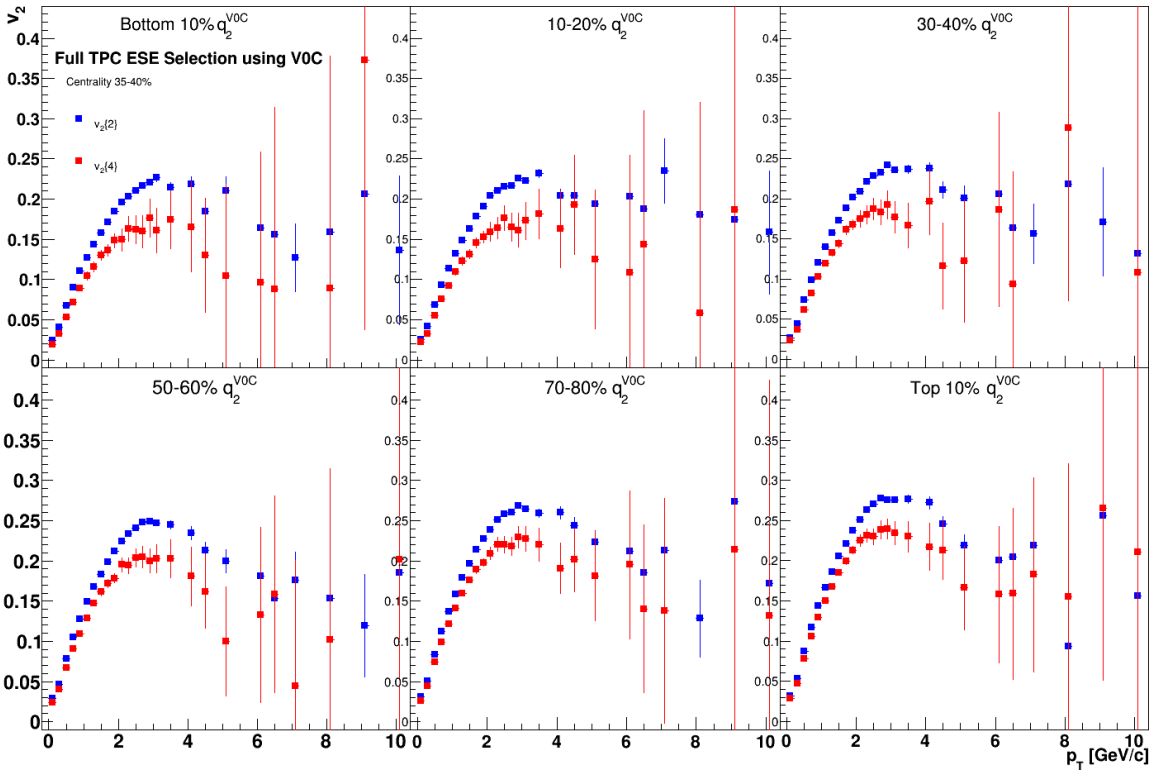

Figure 24: Comparison of measured elliptic flow using two-particle correlations (blue) and four-particle correlations (red) for different q_2^{V0C}-selection intervals.

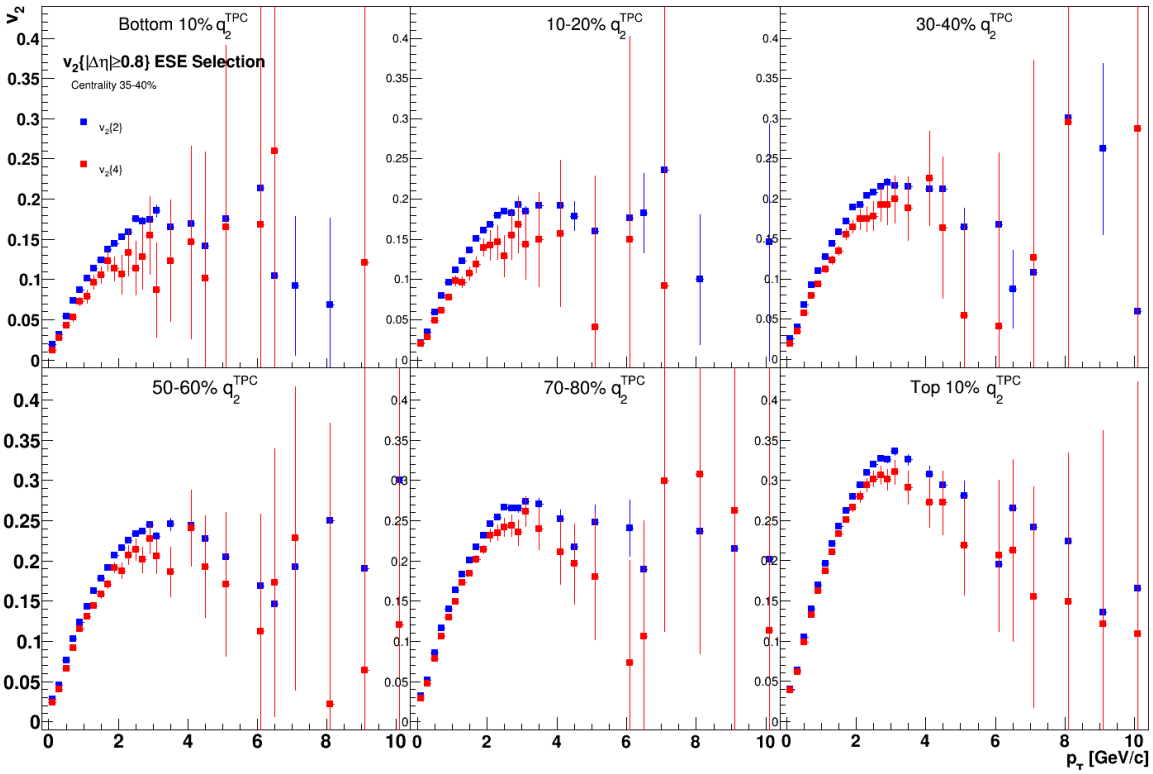

Figure 25: Comparison of measured elliptic flow using two-particle correlations (blue) and four-particle correlations (red) for different $q_2^{\mathrm{TPC}}\{|\eta| < 0.4\}$-selection intervals.

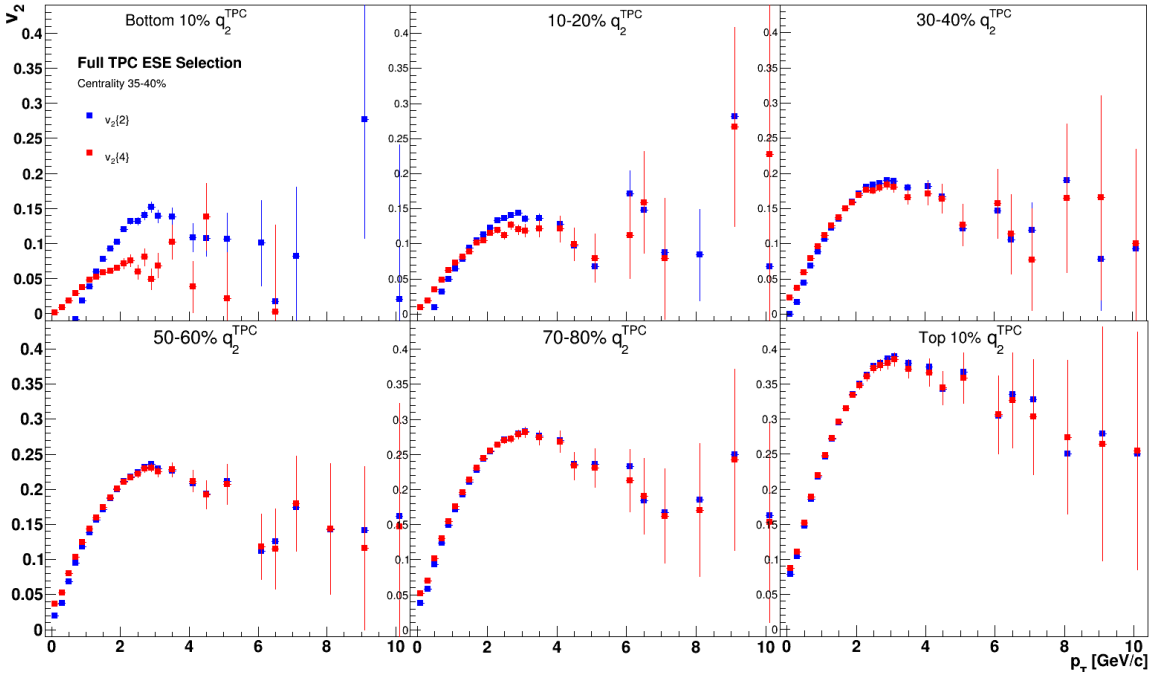

Figure 26: Comparison of measured elliptic flow using two-particle correlations (blue) and four-particle correlations (red) for different q_2^{TPC}-selection intervals.

7.2 Fluctuations and Non-Flow Effects

The measured differences of the two- and four-particle correlations given by $v_2\{2\} - v_2\{4\}$ in the transverse momentum interval $0 < p_{\mathrm{T}} < 5$ GeV/c are shown in Fig. 27 for the three ESE studies. The unbiased v_2 measurements correspond to the difference of the measured two- and four-particle elliptic flow seen in Fig. 20. When the difference is studied for the top 10% q_2-selected events it is seen that the flow fluctuations are reduced compared to the unbiased difference. Especially for the full TPC study it is seen that the difference becomes negative at low p_{T} which corresponds to four-particle correlations measuring a greater elliptic flow than two-particle correlations. The picture in the most circular collision shapes is quite inconclusive as large statistical errors make the results of ESE-selected events indistinguishable from the unbiased events. However, in the full TPC study a highly irregular behaviour in the measured two- and four-particle difference is seen.

Results of the differences of the squares of the measured elliptic flow, $v_2\{2\}^2 - v_2\{4\}^2$, as a function of transverse momentum are shown in Fig. 28. The results compare the difference seen in the most elliptic events with the most circular events. By comparing the three studies it is seen that the difference is largest for selections on q_2^{V0C} suggesting that it provides the worst precisions on the event shapes. It is also again seen that the difference becomes negative at low p_{T} for top 10% q_2^{TPC} events.

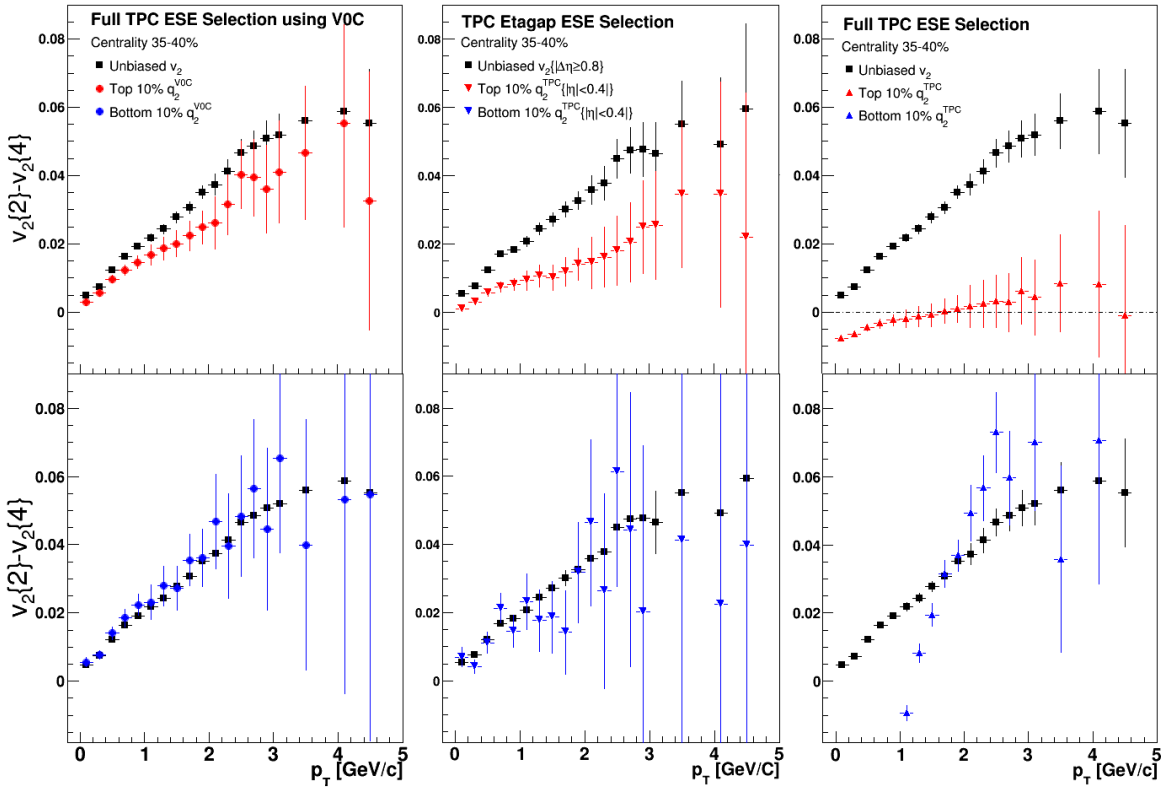

Figure 27: Measured elliptic flow difference between two- and four-particle correlations. Results are presented for three cases with different q_2-vector selecting top 10% and bottom 10% flow events. The results are compared with the measured unbiased difference (no ESE selection).

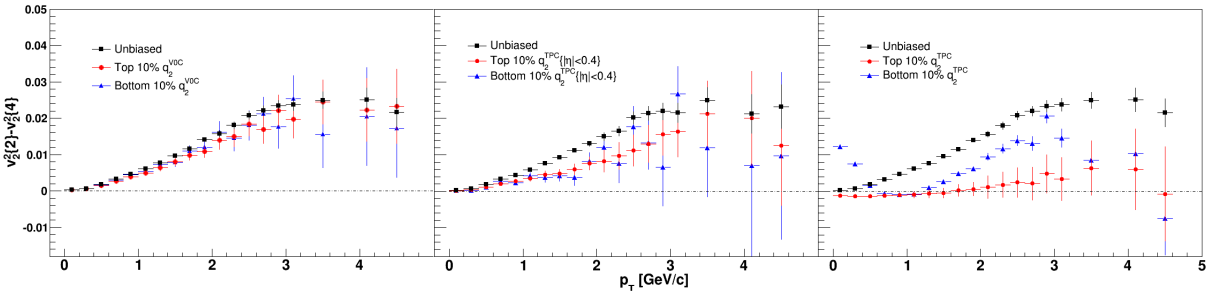

Figure 28: The measured squared elliptic flow difference between two- and four-particle correlations for (red) top 10% q_2-selected and (blue) bottom 10% q_2-selected compared to (black) unbiased. A horizontal line is placed at the vertical zero point to help guide the eye.

8 Discussion of Elliptic Flow Measurements

The results on the measurements of $v_2\{2\}$ and $v_2\{4\}$ suggest that a global property, likely related to the eccentricity of the initial geometry, is selected with the ESE technique. The transverse momentum distributions indicate that events selected with a larger flow-vector, and therefore larger eccentricity, have increased elliptic flow. This holds for all the three studies presented in this thesis and is also in agreement with previous studies that implement the ESE technique [43; 44]. The selection of a global property is further indicated by the calculated ratios between ESE-selected and unbiased measurements. The nearly flat ratios seen in Fig. 21 and 22 extend over the low to intermediate-p_{T} range and suggest a selection that is based on the events initial eccentricity of the collision.

A non-flatness in the ESE-to-unbiased ratio is associated with non-flow correlations seen in the analyzed events. In the high-p_{T} region ($p_{\mathrm{T}} > 5$ GeV/c) there are small observable shifts resolvable from the large statistical uncertainties suggesting non-flow contamination. Large non-flow effects are also seen at low-p_{T} in Fig 23, where the elliptic flow and q_2^{TPC}-vector calculations overlap in the same pseudorapidity interval $|\eta| < 0.8$. The elliptic flow and flow vector are highly correlated in this study and provide some very interesting results. In the event shape selected events with high eccentricity (Fig. 26) it is seen that the four-particle cumulant is larger than the two-particle cumulant. This suggests that the flow fluctuations that are dominated by event-by-event anisotropies are removed and the remaining difference is due to non-flow. It also suggests that the non-flow bias on four-particle cumulants is perhaps not negligible as previously assumed. However, it could also suggest that the correlations between v_2 and q_2 are more important for the 4-particle correlations than the two-particle correlations. When the q_2-selection is applied it selects not only on the initial geometry but also on the fluctuations. Further, the results for the bottom 10% q_2^{TPC}-selection also indicate highly irregular behaviour with a strong discrepancies seen between $v_2\{2\}$ and $v_2\{4\}$. Perhaps this effect originates from events with very strong non-flow correlations. When $v_2\{2\}$ and $v_2\{4\}$ are calculated using the same tracks as q_2 it gives strange results, which can originate from an interplay of flow and non-flow being biased in the same or opposite spatial directions.

The event shape selections using q_2^{V0C} and $q_2^{\mathrm{TPC}}\{|\eta| < 0.4\}$ provide further results to help assess non-flow contribution. The relative flatness seen in the ratio between the ESE-selection and unbiased sample (see Fig. 21 and 22) suggests minimal contribution from non-flow correlations. An intriguing behaviour is that the non-flatness is more pronounced in the four-particle correlations suggesting that non-flow is a bias to the measurement, contrary to what is believed. Still, introducing rapidity-gaps for the v_2 and q_2 measurements is a good way of reducing contributions from short-range correlations, as flow is a large scale effect. The effectiveness is directly seen in the measured ratios at low p_{T} across the three studies.

The discriminating power of the q_2-vector suggests that using the TPC provides better selectivity for the q_2-vector than the V0C detector. This difference can be due to a lower elliptic flow at backward pseudorapidity, where the V0C covers $-3.7 < \eta < -1.7$, compared to the mid-rapidity coverage of the TPC ($|\eta| < 0.8$). There could also be different contributions of non-flow correlations between the measured flow-vector and the elliptic flow. Therefore, when using either q_2^{V0C} or q_2^{TPC} for event shape selection one changes the non-flow and the discriminating power of the flow vector.

The inclusion of the V0C detector in this analysis was motivated by introducing a large pseudorapidity separation between q_2 and v_2 to further suppress and assess non-flow

contributions. However, due to the worsening selectivity of q_2^{V0C} compared to q_2^{TPC} it is difficult to fully suppress the anisotropic flow fluctuations. Further, non-flow correlations are generally assumed to be short-range effects in pseudorapidity (*e.g.* resonance decays) and it is not well understood at what point any extension in the pseudorapidity separation becomes redundant. Further, the V0C detector has a limited granularity in the azimuthal plane by being divided into only 8 sectors and causes bad resolution when applied to q_2 selections. The TPC η-gap, however, shows the best solution for event shape studies as it provides a better resolution for controlling the geometry fluctuations. The TPC study with an η-gap is then the preferred choice for selection on v_2 and the fluctuations given by $v_2\{2\}^2 - v_2\{4\}^2$, with the only limiting factor being a reduction in statistics.

9 Conclusion and Outlook

In this thesis, the ESE technique has been implemented and applied to $\sqrt{s_{\mathrm{NN}}} = 2.76$ TeV Pb-Pb collision data measured by ALICE using the TPC and V0C detectors. Differential elliptic flow measurements using the Q-cumulant method from low to intermediate transverse momentum are in agreement with ALICE results providing validation of the results. The TPC study with a rapidity-gap was shown to be the preferred way to study fluctuations with event shape selections.

There remain few possibilities to extend the analysis done in this thesis. For instance, the ALICE detector has recorded Pb-Pb collisions at $\sqrt{s_{\mathrm{NN}}} = 5.02$ TeV at a greater integrated luminosity providing better statistics to study the physics in the high p_{T} region, ($p_{\mathrm{T}} > 10$ GeV/c). It is suggested that the spectra in this region are dominated by jets and the complicated overlap effects with soft and intermediate p_{T} physics processes, such as elliptic flow, are avoided. By then applying the ESE technique it is suggested that it can provide more insight into the jet quenching phenomena [58].

There is also evidence for QGP formation in high multiplicity p-p and p-Pb collisions from, for instance, observation of collective effects such as elliptic flow [59]. This suggests that p-p collisions either produce a QGP or that the collective effects do perhaps not originate from the medium but from some other pheneomena [60].

As a final remark, I would like to put things into a bigger perspective. The QGP phenomenon was first introduced in this thesis as a state of matter dominated by the strong interactions between quarks and gluons which existed in the early Universe. Evidence for the formation of this plasma in the laboratory was first presented in the 1990s and current research is focused on understanding phenomena such as elliptic flow which can be described by hydrodynamical models. The plasma also functions as a probe into the behaviour of strong interactions and the QCD phase diagram. From a cosmological perspective it would be very interesting if the QGP manufactured in heavy-ion collisions can provide a better understanding to how our Universe have evolved.

References

[1] Itzhak Tserruya. The Strongly Interacting Quark Gluon Plasma at RHIC and LHC. *EPJ Web Conf.*, 70:00022, 2014.

[2] John Adams et al. Experimental and theoretical challenges in the search for the quark gluon plasma: The STAR Collaboration's critical assessment of the evidence from RHIC collisions. *Nucl. Phys.*, A757:102–183, 2005.

[3] I. Arsene et al. Quark gluon plasma and color glass condensate at RHIC? The Perspective from the BRAHMS experiment. *Nucl. Phys.*, A757:1–27, 2005.

[4] K. Adcox et al. Formation of dense partonic matter in relativistic nucleus-nucleus collisions at RHIC: Experimental evaluation by the PHENIX collaboration. *Nucl. Phys.*, A757:184–283, 2005.

[5] M. A. Stephanov. QCD phase diagram: An Overview. *PoS*, LAT2006:024, 2006.

[6] Particle Data Group. *Lawrence Berkeley National Laboratory*, 2015.

[7] Jean-Yves Ollitrault. Anisotropy as a signature of transverse collective flow. *Phys. Rev. D*, 46:229–245, Jul 1992.

[8] Ulrich W. Heinz. The Strongly coupled quark-gluon plasma created at RHIC. *J. Phys.*, A42:214003, 2009.

[9] Ante Bilandzic, Christian Holm Christensen, Kristjan Gulbrandsen, Alexander Hansen, and You Zhou. Generic framework for anisotropic flow analyses with multiparticle azimuthal correlations. *Phys. Rev.*, C89(6):064904, 2014.

[10] Jurgen Schukraft, Anthony Timmins, and Sergei A. Voloshin. Ultra-relativistic nuclear collisions: event shape engineering. *Phys. Lett.*, B719:394–398, 2013.

[11] Sheldon L. Glashow. Partial-symmetries of weak interactions. *Nuclear Physics*, 22(4):579 – 588, 1961.

[12] W. Pauli. Uber das H-Theorem vom Anwachsen der Entropie vom Stand- punkt der neuen Quantenmechanik. *Probleme der modernen Physik*, pages 30–45, 1928.

[13] K. A. Olive et al. Review of Particle Physics. *Chin. Phys.*, C38:090001, 2014.

[14] M. Gell-Mann. A schematic model of baryons and mesons. *Physics Letters*, 8(3):214 – 215, 1964.

[15] E. D. Bloom, D. H. Coward, H. DeStaebler, J. Drees, G. Miller, L. W. Mo, R. E. Taylor, M. Breidenbach, J. I. Friedman, G. C. Hartmann, and H. W. Kendall. High-energy inelastic $e - p$ scattering at 6 and 10. *Phys. Rev. Lett.*, 23:930–934, Oct 1969.

[16] Peter W. Higgs. Broken symmetries and the masses of gauge bosons. *Phys. Rev. Lett.*, 13:508–509, Oct 1964.

[17] O. W. Greenberg. Spin and unitary-spin independence in a paraquark model of baryons and mesons. *Phys. Rev. Lett.*, 13:598–602, Nov 1964.

[18] David J. Gross and Frank Wilczek. Ultraviolet behavior of non-abelian gauge theories. *Phys. Rev. Lett.*, 30:1343–1346, Jun 1973.

[19] Bot. http://cronodon.com/atomic/qcd.html. *Planet Cronodon*, Retrieved May 2017.

[20] Wojciech Florkowski. *Phenomenology of Ultra-Relativistic Heavy-Ion Collisions*. 2010.

[21] V. Khachatryan et al. Measurement of the inclusive 3-jet production differential cross section in proton–proton collisions at 7 tev and determination of the strong coupling constant in the tev range. *The European Physical Journal C*, 75(5):186, 2015.

[22] Bo Andersson, G. Gustafson, G. Ingelman, and T. Sjostrand. Parton Fragmentation and String Dynamics. *Phys. Rept.*, 97:31–145, 1983.

[23] T. D. Lee and G. C. Wick. Vacuum stability and vacuum excitation in a spin-0 field theory. *Phys. Rev. D*, 9:2291–2316, Apr 1974.

[24] Edward V. Shuryak. Theory of Hadronic Plasma. *Sov. Phys. JETP*, 47:212–219, 1978. [Zh. Eksp. Teor. Fiz.74,408(1978)].

[25] Gordon Baym. RHIC: From dreams to beams in two decades. *Nucl. Phys.*, A698:XXIII–XXXII, 2002.

[26] Roman Pasechnik and Michal Šumbera. Phenomenological Review on Quark-Gluon Plasma: Concepts vs. Observations. *Universe*, 3(1):7, 2017.

[27] Johann Rafelski. Melting Hadrons, Boiling Quarks. *Eur. Phys. J.*, A51(9):114, 2015.

[28] Fridolin Weber and Rodrigo Negreiros. Phase Transitions in Dense Baryonic Matter and Cooling of Rotating Neutron Stars. *Acta Phys. Polon. Supp.*, 3:701–710, 2010.

[29] Raghunath Sahoo. Relativistic Kinematics. 2016.

[30] Min He, Rainer J. Fries, and Ralf Rapp. Scaling of Elliptic Flow, Recombination and Sequential Freeze-Out of Hadrons in Heavy-Ion Collisions. *Phys. Rev.*, C82:034907, 2010.

[31] Alexander Colliander Hansen. Pseudorapidity dependence of elliptic flow in pb+pb collisions at $\sqrt{s_{NN}} = 2.76$ tev with alice. Master's thesis, Niels Bohr Institute, 2011.

[32] Stephen J. Sanders Michael L. Miller, Klaus Reygers and Peter Steinber. Glauber modeling in high energy nuclear collisions. *Ann. Rev. Nucl. Part. Sci.*, 57:205–243, 2007.

[33] The ALICE Collaboration. Centrality determination of pb-pb collisions at $\sqrt{s_{NN}} =$ 2.76 tev with alice. *Phys. Rev. C*, 88:044909, Oct 2013.

[34] The ALICE collaboration. Performance of the alice vzero system. *Journal of Instrumentation*, 8(10):P10016, 2013.

[35] A. K. Chaudhuri. *A short course on Relativistic Heavy Ion Collisions*. IOPP, 2014.

[36] Vytautas Vislavicius and Alexander Kalweit. Multiplicity dependence of light flavour hadron production at LHC energies in the strangeness canonical suppression picture. 2016.

[37] Betty Bezverkhny Abelev et al. Production of charged pions, kaons and protons at large transverse momenta in pp and Pb–Pb collisions at $\sqrt{s_{\rm NN}}$ =2.76 TeV. *Phys. Lett.*, B736:196–207, 2014.

[38] Raimond Snellings. Elliptic Flow: A Brief Review. *New J. Phys.*, 13:055008, 2011.

[39] C. Adler et al. Azimuthal anisotropy and correlations in the hard scattering regime at rhic. *Phys. Rev. Lett.*, 90:032301, Jan 2003.

[40] S. Voloshin and Y. Zhang. Flow study in relativistic nuclear collisions by Fourier expansion of Azimuthal particle distributions. *Z. Phys.*, C70:665–672, 1996.

[41] A. Bilandzic. Anisotropic flow analyses with multiparticle azimuthal correlations. *Journal of Physics: Conference Series*, 798(1):012058, 2017.

[42] C. Adler et al. Elliptic flow from two and four particle correlations in Au+Au collisions at s(NN)**(1/2) = 130-GeV. *Phys. Rev.*, C66:034904, 2002.

[43] Jaroslav Adam et al. Event shape engineering for inclusive spectra and elliptic flow in Pb-Pb collisions at $\sqrt{s_{\rm NN} = 2.76}$ TeV. *Phys. Rev.*, C93(3):034916, 2016.

[44] G. Aad et al. Measurement of the correlation between flow harmonics of different order in lead-lead collisions at $\sqrt{s_{NN}}$ = 2.76 tev with the atlas detector. *Phys. Rev. C*, 92:034903, Sep 2015.

[45] Oliver Sim Brüning, Paul Collier, P Lebrun, Stephen Myers, Ranko Ostojic, John Poole, and Paul Proudlock. *LHC Design Report*. CERN Yellow Reports: Monographs. CERN, Geneva, 2004.

[46] J M Jowett, G Arduini, R Assmann, P Baudrenghien, C Carli, M Lamont, M Solfaroli Camillocci, J Uythoven, W Venturini, and J Wenninger. First run of the LHC as a heavy-ion collider. (CERN-ATS-2011-143):3 p, Sep 2011.

[47] Betty Bezverkhny Abelev et al. Performance of the ALICE Experiment at the CERN LHC. *Int. J. Mod. Phys.*, A29:1430044, 2014.

[48] The ALICE Collaboration. The alice experiment at the cern lhc. *Journal of Instrumentation*, 3(08):S08002, 2008.

[49] Christian Lippmann. Upgrade of the ALICE Time Projection Chamber. 2014.

[50] A. Bilandzic and S. Snellings, R.and Voloshin. Flow analysis with cumulants: Direct calculations. *Phys. Rev. C*, 83:044913, Apr 2011.

[51] A. Bilandzic. *Anisotropic Flow Measurements in ALICE at the Large Hadron Collider*. PhD thesis, Utrecht University, 2012.

[52] Nicolas Borghini, Phuong Mai Dinh, and Jean-Yves Ollitrault. Flow analysis from multiparticle azimuthal correlations. *Phys. Rev. C*, 64:054901, Sep 2001.

[53] Alexander Colliander Hansen. *Pseudorapidity Dependence of Anisotropic Azimuthal Flow with the ALICE Detector*. PhD thesis, Niels Bohr Institute, 2014.

[54] Jean-Yves Ollitrault, Arthur M. Poskanzer, and Sergei A. Voloshin. Effect of flow fluctuations and nonflow on elliptic flow methods. *Phys. Rev.*, C80:014904, 2009.

[55] Rene Brun and Fons Rademakers. Root - an object oriented data analysis framework. In *AIHENP'96 Workshop, Lausane*, volume 389, pages 81–86, 1996.

[56] Jr. David A. Moon, Guy L. Steele. GNU Emacs Manual. *GNU Emacs Manual.*, Retrieved May 2017.

[57] K Aamodt et al. Elliptic flow of charged particles in Pb-Pb collisions at 2.76 TeV. *Phys. Rev. Lett.*, 105:252302, 2010.

[58] Peter Christiansen. Event-Shape Engineering and Jet Quenching. *J. Phys. Conf. Ser.*, 736(1):012023, 2016.

[59] Piotr Bożek. Elliptic flow in proton–proton collisions at 7 tev. *The European Physical Journal C*, 71(1):1530, 2011.

[60] Christian Bierlich. Particle production and qgp effects in pp and pa with the dipsy generator.